Carbonic anhydrase inhibitors prevent presymptomatic capillary flow disturbances in a model of cerebral amyloidosis

Eugenio Gutiérrez-Jiménez[1,2,#], Peter Mondrup Rasmussen[1], Irene Klærke Mikkelsen[1], Sreekanth Kura[3], Signe K. Fruekilde[1], Brian Hansen[1], Luca Bordoni[4], Jasper Carlsen[5], Johan Palmfeldt[5], David A. Boas[3], Sava Sakadžić[6], Sergei Vinogradov[7,8], Mirna El Khatib[7,8], Jaime Ramos-Cejudo[9], Boris Wied[1], Desiree Leduc-Galindo[1], Elisa Canepa[10], Adam C. Mar[11], Begona Gamallo-Lana[11], Silvia Fossati[10], Leif Østergaard[1,12]

1. Center of Functionally Integrative Neuroscience, Department of Clinical Medicine, Aarhus University.
2. Department of Biomedicine, Aarhus University.
3. Department of Biomedical Engineering, Boston University, Boston, Massachusetts, USA.
4. GliaLab and Letten Centre, Division of Anatomy, Department of Molecular Medicine, Institute of Basic Medical Sciences, University of Oslo, Oslo, Norway.
5. Research Unit for Molecular Medicine (MMF), Department of Clinical Medicine, Aarhus University, Aarhus N, Denmark
6. Athinoula A. Martinos Center for Biomedical Imaging, Massachusetts General Hospital, Harvard Medical School, Charlestown, Massachusetts, USA.
7. Department of Biochemistry and Biophysics, Perelman School of Medicine, University of Pennsylvania, Philadelphia, PA 19104, USA
8. Department of Chemistry, School of Arts and Sciences, University of Pennsylvania, Philadelphia, PA 19104, USA
9. Department of Psychiatry and Neurology, New York University (NYU) Grossman School of Medicine, New York, NY, USA
10. Alzheimer's Center at Temple, Department of Neural Sciences, Lewis Katz School of Medicine, Temple University, Philadelphia, Pennsylvania, USA
11. Department of Neuroscience and Physiology, Neuroscience Institute, Grossman School of Medicine, New York University, New York, New York, USA
12. Section of Neuroradiology, Department of Radiology, Aarhus University Hospital, Aarhus N, Denmark

Corresponding author

Correspondence to:
Eugenio Gutiérrez Jiménez
Mail: eugenio@cfin.au.dk
Address: Palle-Juul Jensens Blvd. 165, 8200 Aarhus N, Denmark
Tlf.: +45 4086 1281

Summary

To enhance early diagnosis and treatment of Alzheimer's disease (AD), understanding the pathological changes before symptoms arise is crucial. The continuum model of AD suggest that Aβ beta (Aβ) accumulation precedes symptoms by at least 15 years, with vascular changes detectable around this time. Disturbances in capillary flow dynamics have been linked to reduced oxygen delivery to brain tissue, but evidence in presymptomatic AD remains elusive. We examined capillary flow dynamics in presymptomatic Tg-SwDI mice and the capacity of carbonic anhydrase inhibitors (CAIs) to prevent capillary flow disturbances. Our study revealed capillary flow disturbances associated with alterations in capillary morphology, adhesion molecule expression, and Aβ load in cognitively normal 9–10-month-old Tg-SwDI mice. Treated mice showed ameliorated capillary flow disturbances, enhanced oxygen availability, and reduced Aβ load. These findings underscore the importance of capillary flow disturbances in presymptomatic AD and highlight CAIs' potential for preserving vascular integrity in early AD.

Introduction

Alzheimer's disease (AD) is the leading cause of dementia globally, with a prevalence of 46.8 million in 2015[1]. AD prevalence in Europe is predicted to double by 2050[2], underscoring the urgent need for effective preventive, therapeutic, and disease-modifying interventions. However, the biological causes of AD still need to be determined. AD is viewed as a biological and clinical continuum developing gradually over years and involves pathological changes such as amyloid-beta (Aβ) plaques, cerebral Aβ angiopathy (CAA), hyperphosphorylated tau protein aggregation (neurofibrillary tangles), and neurodegeneration[3].

Supporting the continuum model of AD, human biomarker data suggests that Aβ accumulation precedes clinical symptoms by at least 15 years[4]. Therapeutic strategies targeting Aβ have proven efficient in reducing Aβ load but show limited capacity to control disease progression and fail to reverse memory loss[5,6]. This creates a critical need to identify and target early disease mechanisms manifesting years before symptoms arise.

AD pathology and cerebrovascular disease (e.g., CAA) frequently coexist in the elderly, with recent studies highlighting a potential synergistic relationship[7]. Vascular contributions to AD is supported by changes in the brain vasculature detected up to 10 years before symptomatic AD and possibly before Aβ deposits[8]. Consistently, AD shares many risk factors with cardiovascular diseases[9,10]. Evidence from animal models shows vascular changes involving disturbed neurovascular coupling[11,12], blood-brain barrier (BBB) dysfunction[13], vascular oxidative stress[14], and inflammatory damage[15], ultimately reducing cerebral blood flow and limiting oxygen and nutrient access to brain tissue. Regulating local CBF is essential for local oxygen delivery during metabolic demands. Capillary transit time and blood flow distribution across the capillary bed significantly influence oxygen extraction[16]. Disturbances in capillary flow dynamics including transient blockage by leukocytes or platelets[17] and capillary constrictions due to Aβ plaques[18] have been observed in animal models of AD. These disturbances may increase capillary resistance, induce flow distribution disturbances, and reduce oxygen extraction efficiency, termed capillary dysfunction[19].

Recent observations underscore the significance of early disturbances in capillary flow as contributors to AD pathology[19]. Elevated capillary transit-time heterogeneity (CTH) is observed in AD patients and individuals with mild cognitive impairment compared to controls[20] and at preclinical stages[21]. Similarly, a murine AD model exhibits increased CTH in symptomatic stages[11]. However, capillary flow disturbances have not yet been observed during presymptomatic stages of AD.

Therapeutic prevention of abnormal capillary function might be important for AD prevention. Recent studies report that carbonic anhydrase inhibitors (CAIs), potent vasodilators approved for glaucoma[22] and mountain sickness therapy[23], reduce Aβ oligomer neurotoxicity in mouse hippocampus by preventing mitochondrial dysfunction and pro-apoptotic mechanisms[24–27]. We recently examined the effect of long-term CAIs treatment in 15-month-old Tg-SwDI mice, a model of cerebral amyloidosis, and found that CAIs methazolamide (MTZ) and acetazolamide (ATZ) prevent cognitive decline by reducing vascular and total Aβ load, ameliorating glial perivacular clearance and limiting inflammation[28]. However, no studies have examined the effect of CAIs on brain microcirculation in vivo in mouse AD models.

This study aims to determine, first, whether early capillary flow disturbances exist in presymptomatic Tg-SwDI mice, a model of cerebral amyloidosis, and whether those alterations cause capillary dysfunction (increased CTH), and in consequence, impair oxygen uptake. Second, to examine whether early CAI treatment mitigates capillary flow disturbances in presymptomatic Tg-SwDI mice, thus improving oxygen availability, Aβ load, or brain structure.

Using a multiplatform approach, we integrated in vivo optical imaging, molecular biology measurements, and ex vivo MRI to investigate early capillary dysfunction in the Tg-SwDI murine model and the impact of CAI treatment. The Tg-SwDI model is representative of the AD continuum in humans since it shows Aβ accumulation at 4 months but no significant symptoms until 12 months[29]. We demonstrate capillary hemodynamic disturbances in 9-10-months-old presymptomatic Tg-SwDI mice[19,20]. Early CAI treatment, particularly with MTZ, significantly limits capillary flow disturbances, improves oxygen

transport, and prevents Aβ load and pathological brain remodeling. Our findings suggest that CAIs, particularly MTZ, may prevent vascular impairment and slow down AD pathology during presymptomatic stages.

Results

Middle-aged Tg-SwDI mice are characterized by normal memory function, despite showing amyloidosis and cortical hypertrophy

To confirm that 9–10-month-old Tg-SwDI mice are a suitable model of presymptomatic AD, we compared spatial memory and locomotion to those of wild-type (WT) mice, using Barnes maze and open field test. Our results show that the Tg-SwDI mice, at this age, exhibit no cognitive impairment (Fig 1a). Tg-SwDI mice showed a reduction in the distance traveled in the open field test compared to WT, which was not accompanied by other significant locomotor symptoms (Fig 1b). These results are consistent with recent studies that found no cognitive impairment in 9-month-old Tg-SwDI mice[29].

To detect structural, cortical, or hippocampal changes, we estimated regional tissue volumes by ex-vivo magnetic resonance imaging (MRI) in a group of 9-11 months old Tg-SwDI and WT mice. Cortex, hippocampus (HC), somatosensory cortex (SMS), and white matter (WM) were segmented, providing volumes for each region (Fig. 1c). Notably, Tg-SwDI mice did not show signs of atrophy but rather increased cortical volume compared to the WT mice (Fig.1d). These results are consistent with previous observations of whole-brain hypertrophy in another model of cerebral amyloidosis[30]. To detect Aβ burden, we used volumetric two-photon microscopy (TPM) scans and the Aβ fluorescent tracer, methoxy-X04. We confirmed that 9-10 months old Tg-SwDI mice show extensive Aβ burden at 9 to 10 months old (Fig 1e – 1g).

Overall, our analysis of the Tg-SwDI strain in the 9-10 month age range revealed no brain atrophy or cognitive impairment despite the presence of Aβ in the brain tissue, underscoring its suitability as a model for the presymptomatic period of the AD continuum.

Capillary flow disturbances are present in presymptomatic Tg-SwDI mice

We examined presymptomatic Tg-SwDI mice for capillary stalling, a phenomenon linked to reduced CBF in animal models of AD[17,31]. Using optical coherence tomography angiography (OCT-A; Fig. 2a – 2d)[32], we observed an increased number of capillary stalls in Tg-SwDI mice compared to WT mice (Fig. 2e and Supplementary Table 1), including higher incidence (Fig. 2f), prevalence (Fig. 2g), and a suggestive trend towards longer cumulative stall duration ($p = 0.114$; Fig. 2h).

We also examined single capillary hemodynamics using TPM (Fig. 3a). We found a trend towards lower red blood cell velocities (RBCv) in Tg-SwDI mice compared to WT mice ($p = 0.0518$; Fig. 3b). Capillary diameter and cell flux were similar in both groups, suggesting capillary perfusion is maintained, consistent with previous observations in 12-month-old Tg-SwDI mice[33].

A correlation between RBCv and capillary diameter was observed in WT but not in Tg-SwDI mice (Fig. 3f and Supplementary table 2). No correlation was found between cell flux and capillary diameter (Fig. 3g and Supplementary Table 2). The absence of correlation between RBCv and capillary diameter in Tg-SwDI mice may suggest alterations in capillary wall morphology or regulation of capillary blood flow.

Finally, we calculated the coefficient of variance (COV) of RBCv and cell flux, reflecting capillary flow distribution (Fig. 3h and 3i). The Tg-SwDI mice showed a trend toward higher cell flux COV compared to the WT group ($p = 0.0709$; Fig. 3i), suggesting that although capillary perfusion is maintained, disturbances in capillary flow distribution are present.

Disturbed capillary flow dynamics in presymptomatic Tg-SwDI are associated with alterations in capillary morphology

To examine whether capillary flow changes relate to altered capillary morphology, we examined TPM angiograms (Fig. 3j). The mean capillary diameter in Tg-SwDI mice showed no significant difference compared to WT mice (Fig. 3k and Supplementary Table 3). However, Tg-SwDI mice displayed higher variability in capillary diameters, as indicated by the standard deviation (SD) (Fig. 3l) and coefficient of variance (COV) along capillary segments (Supplementary Fig. 2a and Supplementary Table 3). These findings are

consistent with a study that demonstrated capillary constrictions, seemingly mediated by pericytes[34].

We also examined capillary tortuosity, which was similar in Tg-SwDI mice compared to WT mice and not associated with capillary stalls (Supplementary Fig. 2b), consistent with previous observations in the APP/PS1 AD model[17]. Notably, capillary length density and volume were higher in females than in male Tg-SwDI mice. After adjusting for sex, a trend toward lower capillary length density ($p = 0.0672$; Fig. 3m) and volume ($p = 0.0925$; Supplementary Fig. 2c and Supplementary Table 3) was observed in Tg-SwDI compared to WT mice.

Disturbed capillary blood flow dynamics and morphology are associated with increased CTH in presymptomatic Tg-SwDI mice

We measured mean transit-time (MTT) and CTH, the latter serving as an index of capillary dysfunction[35], using indicator-dilution analysis developed for MRI in humans (Fig. 4a)[36] and adopted for TPM (Fig. 4a-4c)[37]. MTT and CTH were measured in two microvascular partitions: one from a pial artery to a vein, best at capturing the vasculature detected within a human MRI voxel, and one from an arteriole to a venule, reflecting the hemodynamics of a smaller subset of capillaries (Fig. 4a).

We observed increased CTH but no changes in MTT between pial arteries and veins in the Tg-SwDI mice compared to WT (Fig. 4e and Supplementary Table 4), suggesting capillary dysfunction in presymptomatic Tg-SwDI mice. These findings are consistent with observations of elevated CTH in presymptomatic AD patients[21]. In healthy vasculature, reductions in CTH accompany shorter MTT, contributing to efficient oxygen extraction at high CBF[37]. However, a strong correlation between MTT and CTH was observed in the Tg-SwDI mice (Supplementary Fig. 3), inconsistent with the WT mice. This correlation between MTT and CTH is characteristic of passive flow regulation[38], suggesting a possible failure in active regulation of capillary flows in Tg-SwDI mice.

Disturbed capillary flow dynamics in presymptomatic Tg-SwDI mice do not affect oxygen extraction fraction (OEF)

To evaluate the impact of Tg-SwDI-related capillary flow disturbances on OEF, we measured in-vivo intravascular partial oxygen tension (pO_2) using the oxygen-sensitive dye PtP-C343 with two-photon phosphorescence lifetime microscopy (2PLM) as previously described[39,40] (Fig. 5a-5b). Manual diameter estimations of scanned pial vessels at the region of 2PLM scans and segmentation of arteries, diving arterioles, upstream venules, and draining veins (Fig. 5c) revealed no discernible diameter differences between Tg-SwDI and WT (Fig. 5d and Supplementary Table 5).

We observed lower pO_2 in the arteries and veins of male Tg-SwDI mice compared to females, and statistical models were thus adjusted by sex. Tg-SwDI mice exhibited significantly lower oxygen saturation (SO_2) in pial arteries compared to WT mice (Fig. 5f and Supplementary Table 6), while pO_2 in pial arteries showed a similar tendency (Fig. 5e and Supplementary Table 6).

In a previous study with young (3-month-old) WT mice, arterial pO_2 was found to increase with arterial vessel diameter[41]. This correlation was also evident in our 9-month-old WT mice, where arterial diameter accounted for approximately 15% of the variability in pO_2 and SO_2 within the arterial network (Supplementary Fig. 4a and 4b). However, this correlation was not observed in Tg-SwDI mice. The absence of a correlation between pO_2/SO_2 with arterial diameter in the Tg-SwDI suggests other compensatory mechanisms, such as blood pressure, may be influencing pO_2 and SO_2 levels in these mice. This observation could also suggest low oxygen tension in brain parenchyma, a major regulator of oxygen diffusion[41], and has been previously observed in a mouse model of AD[42]. No significant differences were found between WT and Tg-SwDI mice in the diameter, pO_2, and SO_2 of veins or venules (Fig. 5g – 5i).

Based on our pO_2 measurements, we estimated OEF by pairing all arteries and veins, and all arterioles and venules where pO_2 measurements were performed. We did not observe differences in the averaged OEF per mouse between groups (Fig. 5j-5k).

Capillary stalling is associated with a higher expression of leukocyte adhesion molecules but not with BBB damage in presymptomatic Tg-SwDI mice

Previous studies have linked AD models and capillary stalling with increased expression of adhesion molecules like intracellular adhesion molecule 1 (ICAM-1)[17], indicative of endothelial activation. Our results show elevated ICAM-1 levels in Tg-SwDI compared to WT, confirming endothelial activation (Fig. 6a). We also measured CypA molecular signature, linked to microvascular damage, including blood-brain barrier breakdown[43], and assessed plasmatic levels of vascular endothelial growth factor A (VEGF-A), an essential pro-angiogenic factor associated with capillary stalling[31]. In contrast to the increase in ICAM-1, tissue CypA and plasmatic VEGF-A levels remained similar between groups (Fig. 6b and 6c).

Presymptomatic Tg-SwDI mice treated with Methazolamide showed normal cortex volume

We administered CAIs, ATZ (Tg+ATZ), and MTZ (Tg+MTZ) to separate groups of Tg-SwDI mice through the diet from 4 months old. Spatial reference memory, assessed with Barnes maze, showed no discernible effects of the treatments at 9-10 months, noting that Tg-SwDI and WT animals showed similar memory functions at this time (Fig. 1a). However, both treated groups exhibited locomotor impairment compared to the WT mice, similar to non-treated Tg-SwDI mice as evidenced by reduced distance traveled (Fig. 1b).

Notably, both treated groups did not show increased brain cortical volume found in untreated Tg-SwDI mice (Fig. 1d).

CAIs prevent capillary flow disturbances in presymptomatic Tg-SwDI mice

In contrast to the alterations found in untreated presymptomatic Tg-SwDI mice, mice treated with MTZ showed similar numbers (Fig. 2e), incidence (Fig. 2f), prevalence (Fig. 2g), and cumulative stall duration to WT mice. However, ATZ-treated mice showed a similar number, incidence, and prevalence of stalls as non-treated Tg-SwDI mice (Fig. 2e – 2g). Both treatments prevented prolonged cumulative stalling time (Fig. 2h). Thus, our data suggests that CAI treatment reduces the net time capillaries are affected by stalling; MTZ more so than ATZ.

When measuring single capillary hemodynamics, Tg+MTZ, and Tg+ATZ mice exhibited higher RBCv, cell flux, and capillary diameter compared to Tg-SwDI mice, with no significant difference in cellular linear density (Fig. 3b – 3e). A clear relationship between RBCv and diameter, similar to WT, was evident for both treatment groups (Fig. 3f), suggesting that patent capillary perfusion in the CAI-treated groups. Unlike WT and Tg-SwDI groups, CAI-treated mice showed a correlation between cell flux and diameter, likely attributed to the vasodilatory effects of the drugs (Fig. 3g). The coefficient of variance (COV) of RBCv and cell flux, reflecting capillary flow distribution, showed lower RBCv COV in ATZ-treated mice compared to WT and non-treated Tg-SwDI mice (Fig. 3h), with a similar effect in cell flux COV compared to non-treated Tg-SwDI mice (Fig. 3i). This more homogenous capillary flow and speed in ATZ-treated mice may help facilitate uniform oxygen distribution, potentially enhancing oxygen extraction[44].

CAIs prevent abnormalities in capillary morphology in presymptomatic Tg-SwDI mice

There was no significant effect of CAIs on capillary diameter along segments (Fig. 3k), suggesting that age-related reduction of capillary diameter previously observed in 15-month-old Tg-SwDI mice[28] is not manifest at 9-10 months. However, we noted a reduction in diameter variability, as evidenced by diameter SD (Fig. 3l and Supplementary Table 3) and diameter COV (Supplementary Fig. 5a and Table 3). These observations suggest that the capillary lumen along the segments exhibited fewer narrowing regions in the treated groups. MTZ-treated mice showed a decrease in capillary density compared to WT mice but this was not significant compared with other Tg groups (Fig. 3m and Supplementary Table 3). Tissue oxygen availability is a main determinant of capillary density, as exemplified by the angiogenesis that accompanies reduced tissue oxygen tension[45]. This effect may explain the lower capillary density in mice treated with MTZ. Overall, these findings highlight the potential influence of CAIs in preserving capillary morphology in Tg-SwDI mice.

MTZ treatment prevents capillary dysfunction and improves oxygen availability in presymptomatic Tg-SwDI mice

MTZ treatment was associated with lower CTH levels than the ATZ-treated mice (Fig. 4e and Supplementary Table 4). ATZ-treated mice tended to show increased CTH from arteriole to venule, but not from artery to vein (Fig. 4d-e and Supplementary Table 4).

Intravascular measurements revealed lower SO_2 levels in the pial arteries of treated groups compared to WT mice and lower pO_2 in ATZ-treated mice (Fig. 5e, 5f, and Supplementary Table 6). Similar pO_2 and SO_2 levels were in diving arterioles of all groups, except for MTZ-treated mice who showed lower SO_2 compared to WT (Fig. 5f and Supplementary Table 6).

MTZ-treated mice showed lower OEF than other transgenic groups (Fig. 5j and 5k). Thus, OEF measured between arteries and veins in MTZ-treated mice was significantly lower than in mice treated with ATZ (Fig. 5j and Supplementary Table 6). Similarly, between diving arterioles and ascending venules, OEF was significantly reduced in MTZ-treated mice compared to non-treated Tg-SwDI and ATZ-treated mice (Fig. 5k and Supplementary Table 6).

Since MTZ-treated mice are presymptomatic, these results imply that oxygen availability exceeds metabolic demands in these animals, even though their lower capillary length density (Fig 3m) reduces total capillary surface area and thereby blood-tissue oxygen exchange. Our data show that increased RBC flux through individual capillaries (Fig. 3c) provides higher oxygen availability in MTZ-treated animals and that increased surface area of individual capillaries (increased diameter, cf. Fig. 3e), homogeneous blood flow distribution across capillary paths (Fig. 4e), and shortened capillary stalls (Fig. 2h) counteract the negative effects of lower capillary length density on blood-tissue oxygen exchange in the resting state.

CAIs reduce ICAM-1 expression and Aβ load in presymptomatic Tg-SwDI mice

CAI-treated groups exhibited a trend towards a lower expression of ICAM-1 compared to non-treated Tg-SwDI mice, with statistical significance in mice treated with ATZ, particularly in the cortex (Fig. 6a). We did not observe differences between groups in CypA or VEGF-A (Fig. 6b and 6c).

In our previous study, CAI treatment prevented Aβ deposition in 15-month-old Tg-SwDI mice[28]. TPM measurements revealed a tendency for reduced Aβ plaques in ATZ-treated mice (Fig. 1g) without discernible alterations in total Aβ burden (Fig. 1f). We conducted a *post hoc* categorization of the population into quartiles based on plaque volume, noting a lower number of very small and small Aβ particles in ATZ-treated mice compared to non-treated mice (Supplementary Fig. 5).

To further address the treatments' impact on Aβ load, we quantified total Aβ-40 and Aβ-42 by conducting ELISA of homogenized cortex and hippocampus. Our analysis revealed lower levels of Aβ-40 and Aβ-42 load in the cortex and hippocampus of female mice. With sex-adjusted analysis, mice treated with ATZ exhibited a reduced Aβ-40 load in the cortex compared to non-treated mice and in the hippocampus relative to Tg-SwDI and MTZ-treated mice (Fig. 7a and Supplementary Table 7). Both treatment groups displayed a lower Aβ-42 load in the cortex and hippocampus (Fig. 7b and Supplementary Table 7).

Discussion

This study provides insights into microvascular dynamics, capillary morphology, and Aβ load in presymptomatic, 9-10-month-old Tg-SwDI mice with cerebral amyloidosis. Our first main finding is that early microvascular changes, such as capillary stalling, increased CTH, and changes in capillary morphometry, coexist with extensive Aβ accumulation before cognitive impairment. These changes are associated with endothelial activation, potentially leading to insufficient oxygen delivery to brain tissue as the model ages. Our second main finding is that long-term CAI treatment prevents microvascular disturbances, so treated mice had similar capillary morphometry to WT mice, reduced Aβ load, and fewer and shorter stalling events, possibly due to reduced endothelial activation.

Alterations in brain hemodynamics are present in AD patients[46–48] and different studies have proved that disturbances in capillary flow dynamics exist in AD models once cognitive impairment is established[31,42,49]. Our study extends these findings by demonstrating that capillary flow disturbances with pronounced alterations in RBCv, cell flux, and capillary stalling are present in presymptomatic mice with cerebral amyloidosis.

Observations of normal CBF during steady-state conditions in 12-month-old Tg-SwDI mice[33] suggest that the capillary disturbances observed in our study may precede reductions in CBF in the Tg-SwDI model, similar to those observed in AD patients during the prodromal phases[20,50]. However, our study cannot confirm this hypothesis. Therefore, longitudinal studies addressing capillary flow disturbances at stages of the disease are necessary to understand the progression of capillary flow disturbances during the development of AD.

Capillary dysfunction is defined as a condition where capillary flow disturbances limit brain oxygen extraction[35]. We measured two indices of capillary dysfunction: cell Flux COV and CTH. The trend observed in presymptomatic Tg-SwDI towards increased cell flux COV suggests that capillary dysfunction is present in this model. We acknowledge that our interpretation based on this value is limited by the low number of capillaries scanned per mouse. We overcame this limitation by using an indicator-dilution method to calculate CTH, confirming capillary dysfunction in the Tg-SwDI mice. Interestingly, the capillary dysfunction was not matched by the expected increase in OEF. The lack of changes in OEF could be due to the lower arterial SO_2 observed in the Tg-SwDI mice, which may indicate low tissue oxygen tension in regions surrounding large vessels, as previously observed in another mouse model of AD[51]. Studies addressing capillary flow dynamics and tissue oxygen tension are necessary to demonstrate that capillary dysfunction leads to low oxygen tension.

The mechanisms behind capillary dysfunction in AD are not well understood and require exploration of major mechanisms controlling capillary flow dynamics, such as hematocrit, capillary diameter, length, and vessel stiffness[52]. The observed correlation between RBCv and cell flux with diameter in WT and treated groups confirms the importance of capillary diameter in capillary flow dynamics. In contrast, the absence of this correlation in the Tg-SwDI mice suggests altered capillary regulation in this model. Instead, they appear to act as passive and rigid vessels, leaving the regulation of RBCv and cell flux to systemic mechanisms, such as heart rate or blood pressure. This is supported by our analysis of capillary morphometry, revealing increased variability in capillary diameter across segments in Tg-SwDI mice. The substantial variability suggests the presence of narrower

segments in the lumen of these mice, reminiscent of capillaries in the brain tissue of AD patients[34]. Such characteristics are associated with rigid pericytes, primary regulators of capillary diameter[34]. Narrowing capillary lumen restricts leukocyte passage, requiring them to change their shape to a disk shape for passage, which increases the contact surface of leukocytes to the capillary wall, thus increasing the number of ligand-receptor bonds and inducing significant expression of adhesion molecules[53]. These assumptions are supported by the overexpression of ICAM-1 in the Tg mice, suggesting that a combination of narrowed capillaries and endothelial activation might explain the increased capillary stalling frequency and cumulative stalling time observed in presymptomatic Tg-SwDI mice. Ultimately, we hypothesize that this scenario increases the resistance of the affected capillaries, leading to capillary blood flow shunting and capillary dysfunction (Fig. 8).

Our previous work shows that long-term treatment with CAIs delays AD phenotype development in animal models without toxicity[24,28]. We observe that CAI-treated mice exhibited increased RBCv and cell flux compared to non-treated Tg-SwDI mice, along with low variability in capillary diameter and a combined trend toward lower expression of ICAM-1 in brain cortex. These results are consistent with the reduction in capillary stalling time. Importantly, mice treated with MTZ showed larger capillary diameters than the non-treated Tg-SwDI and WT mice, without any difference in pial vasculature or diving vessels. In cortical microvasculature, capillaries and arterioles work together to secure blood flow distribution across the microvasculature, and capillary dilation and constrictions offer an efficient mechanism for local blood flow and oxygen delivery regulation across the capillary bed[54]. Resistance to blood flow decreases with vessel dilation[52], and widespread capillary dilation further leads to a global decrease in vascular resistance and, hence, increased CBF under a given perfusion pressure. Based on the increased capillary diameters in MTZ-treated mice coupled with the expected increase in brain perfusion and understanding that hypoxia is the primary driver of angiogenesis, we propose that tissue oxygenation is enhanced in the MTZ group. This aligns with the reduction of capillary density in the MTZ-treated mice noted in our morphometric analysis of capillary networks. These observations suggest that decreased capillary resistance is crucial for the treatment's efficacy in preventing capillary flow disturbances in Tg-SwDI mice, facilitating

enhanced oxygen delivery to the brain tissue and potentially preventing new vessel formation.

We demonstrate the preventive effect of CAIs, particularly MTZ, on the development of capillary dysfunction (increased CTH). In healthy vascular networks, as observed in WT mice, an increase in MTT (CBF reduction) is compensated by a reduction in CTH, which is predicted to result in more efficient oxygen extraction[16]. We observed that the microvascular dynamics of MTZ-treated mice resemble WT mice, maintaining adjustments of CTH whenever MTT increases. In contrast, non-treated Tg-SwDI and ATZ-treated Tg-SwDI mice showed a strong correlation between CTH and MTT. Altogether, our results suggest that MTZ prevents disturbances in capillary morphology and flow dynamics, thereby mitigating limitations on oxygen availability to the brain tissue. However, further studies on the effect of CAIs on brain parenchyma oxygenation and the active mechanism of capillary flow regulation (e.g., pericytes) are necessary to further examine the effect of CAIs in capillary flow regulation and oxygen diffusion in AD.

Previous studies have examined vasodilator treatment in a different AD mouse model and found no improvement in symptoms[55]. However, CAIs effectiveness in AD is driven not only by vasodilatory effect but also by prevention of mitochondrial dysfunction, inhibition of pro-apoptotic mechanisms, amelioration of glial reactivity markers, and activation of anti-inflammatory microglia, which we have previously reported[24–27,56]. These factors provide a healthy brain environment capable of more efficient degradation of Aβ. This effect is consistent with the reduction of Aβ load in brain tissue observed here and previously[28]. Notably, we observed that treatment with ATZ showed an ambivalent effect, preventing Aβ load but only with limited improvement in capillary hemodynamics. This effect might be related to known secondary effects of AZT, such as impairment of the diaphragmatic muscle function, causing reduced exercise capacity[57] and its association with increased risk of renal failure[58].

The increased cortical volume in Tg-SwDI mice aligns with previous observations in young mice of another cerebral amyloidosis model[30]. That study suggested mechanisms like hypoperfusion, Aβ-driven neuronal hypertrophy, or astrogliosis could explain the apparent

increase in cortical thickness[30]. Notably, Tg-SwDI mice treated with CAIs did not show a significant increase in cortical volume, suggesting a therapeutic effect of CAIs modulating these hypertrophy pathways. Further studies using advanced MRI analysis are necessary to understand the mechanism behind the increase in cortical tissue in AD mouse models.

Our study is limited by the lack tau pathology in the model used. Studies examining capillary flow dynamics in models with both Aβ and Tau would provide further data on the effects of capillary flow disturbances and dysfunction in the development of AD.

In conclusion, our study shows capillary dysfunction before cognitive impairment in an animal model of cerebral amyloidosis, closely associated with the microstructural capillary changes causing hemodynamic disturbances and brain remodeling, highlighting their potential as early-stage AD biomarkers. Furthermore, our investigation demonstrates that long-term treatment with CAIs, particularly MTZ, can decelerate the development of capillary dysfunction and brain remodeling associated with hemodynamic changes and amyloidosis in AD. These findings underscore the potential of capillary dysfunction as a therapeutic target to slow AD pathology and suggest CAIs as repurposed therapeutic agents.

Methods

Experimental models

The Danish Ministry of Justice and Animal Protection Committees approved all animal procedures and treatment, with the Danish Animal Experiments Inspectorate permit 2017-15-0201-01241. We used adult homozygous mice from the Tg-SwDI line (C57BL/6-Tg(Thy1-APPSwDutIowa)BWevn/Mmjax; MMRRC Stock No: 34843-JAX, The Jackson Laboratory). A group of homozygous breeders was acquired from Jackson Laboratory and bred at the animal facility at the Biomedicine Department, Aarhus University). Animals were of both sexes. A group of control wild-type mice (C57BL/6J) were acquired from Jackson Laboratory, matching sex and age. After weaning from the breeder, mice were transported to the stable facility at the Center of Functionally Integrative Neuroscience (CFIN, Aarhus University). Mice were housed in group cages (between 3 - 5 mice/cage) with *ad libitum* access to water and a standard diet/treatment diet. Mice maintained at

12h:12h light-dark cycle at constant temperature and humidity (21 °C ± 2 and 45% ± 5 relative humidity). Behavioral studies were performed on mice of the same groups, sexes, and age, at NYU School of Medicine, following institutional and National Institutes of Health (NIH) guidelines as in previous work[28], and the animal protocol was approved by the Animal Studies Committee.

Treatment randomization

For treatment with CAIs, a special diet was designed with either acetazolamide (ATZ; Santa Cruz Biotechnology, Inc. Dallas, Texas, USA) or methazolamide (MTZ; Santa Cruz Biotechnology, Inc. Dallas, Texas, USA). Medication was added at a concentration of 0.01% (100 parts per million), corresponding to 20 mg/kg/day, to a standard diet (Altromin 1320; Brogaarden ApS, Lynge, DK). The three specialized diets were produced with the same pellet form. Groups of female and male mice were assigned to three treatment groups with a specialized diet containing either methazolamide (Tg+MTZ), acetazolamide (Tg+ATZ), or placebo (standard diet – Tg-SwDI). The groups were randomized, and the researchers involved in the scans were blinded to the treatment. Previous reports have shown that vascular impairments[59] are already present in the Tg-SwDI mice at the age of 3 months. Thus, we anticipated that starting the treatment at 4 months old would slow the vascular impairment in the treated groups. The treatment lasted six months, and the scans were performed when the mice were between 10 and 11 months. We aimed to conduct the experiment on four groups of mice: WT mice (C57BL/6J, N=16 (F = 8, M = 8)], Tg-SwDI mice treated with MTZ (Tg+MTZ, N=16 (F = 8, M = 8)], Tg-SwDI mice treated with ATZ (Tg+ATZ, N=16 (F = 8, M = 8)] and untreated Tg-SwDI mice (Tg-SwDI, N=16 (F = 8, M = 8)].

Behavioral tests

During the dark phase of the light cycle, mice underwent a behavioral test battery. Animals were acclimated to the testing room for at least 30 minutes prior to each session. All experimental procedures were performed at NYU Langone's Rodent Behaviour Laboratory and adhered to the guidelines of the NYU School of Medicine's Institutional Animal Care and Use Committee.

Barnes maze

The Barnes maze assesses visuospatial learning and memory in mice. The test comprises a raised beige platform (91.5 cm in diameter), with a textured surface, positioned 91.5 cm above the ground, which features 20 evenly spaced holes around the edge, each 5 cm wide, located 2.5 cm from the perimeter. Underneath one of these holes, a gray plastic escape box (10×8.5×4 cm) was placed, and its position was kept consistent throughout trials. The placement of the target hole was varied among subjects or groups to ensure balanced spatial conditions. Visual cues were positioned in the testing environment and remained constant across the testing period. Illumination was provided by an overhead lamp (600 lux) positioned above the center of the maze. Over 7 consecutive days, mice underwent 12 trials: one habituation trial on day 0, 10 training trials spanning days 1 to 5 (2 trials/day), and the final probe trial on day 6. During the habituation phase, mice were introduced to the maze under an inverted, clear 500 ml beaker for one minute, accompanied by white noise. Subsequently, the beaker was slowly lifted to reveal the target hole, allowing the mouse to explore the escape box for two minutes. Following a 2-hour intertrial interval (ITI) of habituation, standard training trials commenced, with each day featuring two trials; the animal was placed in the center of the maze in a plastic (15×15×20 cm) start box, with a white noise stimulus applied. After 10-15 seconds, the box was lifted, and the animal was given a three-minute window to locate and enter the designated escape hole. Upon successful entry, the white noise ceased, and the mouse was left in the escape box for one minute, and then moved to the home cage. If the mouse failed to find the escape hole within the allotted time, it was gently guided to the target hole beneath the inverted beaker, and left there for one minute, with white noise off. On each training day, trials were separated by 1.5 to 2-hour ITIs, with the maze platform rotated in each trial. On the sixth day, a two-minute probe trial was conducted, similar to training trials, except that the escape box was removed. Behavior was recorded via an overhead camera for subsequent analysis, using Noldus Ethovision software (11.5 version). Key metrics, including distance traveled and number of non-target holes visited, were measured as indicators of spatial memory and then plotted accordingly.

Open-field test

The open-field test was employed to evaluate animal locomotor activity patterns. The test occurred within a novel open-topped white acrylic enclosure, measuring 40x40x40 cm, with uniform overhead lighting (110-130 lux). Mice were individually introduced into a corner of the arena and given 15 minutes to freely explore. Video of the 30-minute sessions were recorded from an overhead camera, and subsequently analyzed (Noldus Ethovision XT 11.5 software). Locomotor activity parameters, such as total distance traveled, speed, moving time, and time spent in the central zone (20x20 cm) were recorded, and hence plotted.

Surgical preparation and training of animals for optical imaging in the awake state

A chronic cranial window was surgically implanted over the somatosensory area of the barrel cortex (S1bc), as previously described[60]. A chronic cranial window was surgically implanted over the somatosensory area of the barrel cortex (S1bc), as previously described[60]. To minimize stress and enhance recovery, mice were acclimated to handling for 5 days prior to the surgical preparation. On the day of the surgery, mice received a subcutaneous injection of dexamethasone (4.8 mg/kg; BRAND) to reduce brain post-surgical brain edema. The surgical procedure was performed under anesthesia with 1.75 – 2% Isoflurane (induction with 3%) with 100% O_2 flow through a face mask. Subsequently, intraperitoneal injections of ampicillin (200 mg/kg) and carprofen (10 mg/Kg) were administered for antibiotic and anti-inflammatory/pain-killer relief purposes, respectively. Lidocaine was applied under the scalp for local anesthesia and eye ointment was applied to both eyes. During the whole surgery, the mouse was securely mounted on a stereotaxic frame (RWD Life Science Co., LTD, Shenzhen, Guangdong, China). A cranial window of ~3mm in diameter was centered over the region of S1bc representing the whisker C2 (1.5-2 mm anterior-posterior, 3 mm mediolateral). The cranial window was covered with an in-house glued glass plug consisting of one 5-mm and three 3-mm cover glasses. The glass plug was secured to the skull applying cyanoacrylate glue around the edges (Loctite Super Glue gel, Loctite® Brand, Westlake, Ohio, USA). A custom-made head-bar was affixed and glued onto the frontal area of the skull and the whole exposed area of the skull was covered with a layer of dental cement (Meliodent, Kulzer. Hanau, Germany). After surgery, mice were recovered in a heated recovery chamber and were closely monitored until voluntary movement was observed. Subsequently, each mouse was moved back to its

own housing box. We continued to monitor their recovery for a period of 5 days post-surgery, providing antibiotic and anti-inflammatory medication as needed. Acclimatization with handling continued through the post-surgical period to minimize stress and improve training sessions.

After the post-surgical period, mice underwent daily training sessions for awake imaging periods of ~2.5 hrs. Each mouse began with 15-minute training sessions, gradually increasing the duration by 15 minutes in subsequent sessions until the target training duration was achieved. Training involved using a replica of the custom-built frame that was employed for optical imaging.

We placed a tail catheter for infusion of fluorescent dyes to label the plasma for TPM scans. For this procedure mice were lightly anesthetized with Isoflurane 1.2% delivered through a face mask (100% O_2 flow). A catheter was assembled with a PE10 tube attached to a 50 unit (500 µl) insulin syringe on one side and a 30G Monoject needle (Covident) on the opposite side. The catheter was filled with a 5% heparin (LEOPharma) solution. The catheter was placed on one of the lateral tail veins, after warming up the tail and applying ethanol to induce vasodilation. The catheter was fixed with dental cement (GC-Fuji-Plus, GC Corporation, Japan) to avoid movement or detachment during the scanning period. After the scanning session, the catheter was gently removed and the tail was gently pressed until bleeding stopped.

Optical imaging acquisition

We performed imaging in awake head-restrained mice using a frame equipped with a head-holder and a fabric cradle where the mouse could rest in a relaxed position.
Optical coherence tomography (OCT). For OCT imaging, we applied a spectral-domain OCT system (1310 nm center wavelength, bandwidth 1700 nm, Telesto II, Thorlabs, Inc. Newton, NJ, USA). This system provides an axial resolution of ~3.5 um and an imaging speed of ~47,000 A-scan/s. To achieve a transverse resolution of ~1.5 µm, we used a 10X near-infrared (NIR) objective (Mitutoyo Corporation, Kawasaki, Kanawaga, Japan). We acquired time-series OCT-angiograms, each consisting of 400 x 400 pixels (600 μm^2), using the decorrelation method[61]. In our setup, each OCT-angiogram acquisition took ~8.5

s with a buffering time of 5 s between OCT volumes. Sixty volumes of the cortical microvasculature were acquired in each ROI.

Detection of capillary stalls from post-processed data

After postprocessing the OCT-angiograms, a volume of 30 pixels was selected 135 - 225 µm beneath the brain surface and was projected as maximum intensity projection (MIP) for analysis. In OCT imaging, stalling events are considered capillaries without perfusion during an OCTA volume. OCT signal relies on the movement of particles and light path interference. Each volume represents ~8.5 seconds of capillary dynamics. Stalled capillaries typically re-perfuse within one or two volumes, although some stalls may last longer. We identified capillary stalling events using the graphical user interface (GUI) 'CapStall' designed in MATLAB (Mathworks) that allowed a semiautomatic identification of the stall events[32]. For postprocessing, two research assistants, blinded to the treatment randomization, inspected all images in a time series (volume scanned as a function of time) to identify all image frames in which the capillary segments stalled (Fig. 2a – 2c). After having done the identification of stalling capillaries, a stall-o-gram was plotted. Stall-o-grams (Fig. 2d) depicted the capillary stalls and the stalling frequency during the 60 (1 volume = 8.5 seconds) volumes scanned. For statistical analysis, the assistants manually quantified the capillaries examined in each MIP using Image J and a MATLAB script to calculate the following parameters:

a) Total of identified capillary stalls.
b) Incidence rate, defined as the fraction of capillaries showing a stall episode during 8.5 minutes (sixty 8.5-second volumes).
c) Point of prevalence, which is the average number of capillary stalling episodes per volume (8.5 seconds).
d) Cumulative stall time, representing the cumulative fraction of stalling time relative to the total scanning time (~8.5 minutes).

Two-photon imaging

All two-photon microscopy (TPM) imaging experiments were performed using a Bruker Ultima-IV two-photon laser scanning microscope (Brucker Corporation, Billerica, MA, USA) and Praire View Software version 5.1 (Brucker Corporation, Billerica, MA, USA). Excitation

of fluorescent dyes was performed with a tunable Ti:Saphire laser Chameleon (Coherent, Santa Clara, California, USA). Fluorescence emission was detected by two GaAsP photomultiplier modules (Hamamatsu, H10770. Hamamatsu City, Japan). We used an Olympus 10x water immersion objective (0.3 numerical aperture – NA), 3.3 working distance – WD) to image a 1.18 mm^2 FOV for bolus tracking, intravascular pO2 estimations, and reference angiograms for bolus tracking. We used an Olympus 20x water immersion objective (1.0 NA, 3.00 mm WD) for capillary line-scans, high resolution z-stacks for angiograms, and Aβ plaques. To avoid any effect of temperature on brain hemodynamics, we heated the objective lens with an electric heater (TC-HLS-05, Bioscience Tools) to maintain the temperature of the water between the cranial window and the objective lens at 36–37°C.

Two imaging sessions were performed, interleaving one day between scans to reduce stress induced by repetitive sessions. All scans were performed during steady-state conditions. On the first day of TPM imaging, we acquired measurements of brain hemodynamics in awake-restrained mice. The second day was performed under slight anesthesia (0.9 – 1% Isoflurane) delivered through a face mask to acquire morphological data (i.e., angiograms, Aβ plaques).

We performed the following TPM acquisition sequences:

1) Indicator-dilution technique (Bolus tracking): We estimated MTT and CTH applying an indicator-dilution methodology as previously described[37]. This methodology relies on the detection of concentration-time-curves (CTC) during the passage of a bolus of fluorescent dye from the arterial to the venous network. Each bolus was injected through the tail catheter using an infusion pump (GenieTouch; KenScientific, Torrington, USA) set at an infusion rate of 20 μL/s. To avoid pain due to the I.V. infusion of cold solutions, we kept the catheter warm with a rubber tube attached to a standard heating circulation bath (ThermoScientific, Walthman, USA). To locate the ROI we identified the shadows of the pial vessels detecting NADH-autofluorescence (820 nm excitation). The autofluorescence signal was filtered with a 460 ± 25 nm bandpass filter (Chroma Technology, USA). The volume of the catheter was ~60 μl, and was filled with heparin solution before the scan; therefore,

we habituated the mice to the bolus injection ~6 times (10 µl boluses) before performing the recording paradigm to fill up the catheter with the fluorescent dye. We identified arterial and venous networks during the habituation paradigm. Each bolus consisted of 10 µl of the fluorescent dye Texas-Red dextran (70,000 M.W.; Thermo Fischer Scientific, USA). The signal was filtered with a 605 ± 35 nm bandpass filter (Chroma Technology, USA). We identified an ROI as an area where both pial arteries and veins converged, and a large region with capillaries was observed (Fig. 4a). Each bolus was infused after 7 seconds from the initiation of a time-series of 2D spiral scans with a spatial resolution of 256 x 256 (pixel size = 2.30 µm) which yielded a frame rate of ~6.98 frames-per-second (fps). A total of 3 boluses of each mouse were included for analysis.

2) Intravascular pO_2 measurements: After the placement of the tail catheter, a bolus of ~40–50 µl (10–15 µM final concentration in the blood plasma) of the phosphorescent probe PtP-C343 (MW ~32,000)[39]. Using the residual green fluorescence of the C343-antenna fragments in PtP-C343, we performed a raster scan to map the pial vessels and quantify their diameter. The fluorescent signal was detected with a PTM and passed through a 525 ± 25 nm bandpass filter. We used the PointScan mode of the TPM software to obtain single-point measurements within the luminal side of the arterial and venous networks of the most superficial layers of the brain cortex. We aimed to include two points per vessel in the same vessel detected during the indicator-dilution scans (Fig. 5a). Upon excitation at a single point during 10 µs (820 nm, ~10 mW average power with beam modulation off), the phosphorescence output was passed through a 680 ± 30 nm bandpass filter and collected during 290 µs by a PMT module (H10770PA-50; Hamamatsu), as previously described[40]. For O_2 estimates, we averaged ~15,000 phosphorescence decays per point. Quenching of the probe's phosphorescence is dependent on the O_2 concentration. Therefore, the phosphorescence lifetimes in arteries are expected to be shorter than in veins (Fig. 5b). Two trials per mouse were performed.

3) Line-scans for capillary scans: After the indicator-dilution scans, the remaining volume required to reach 200 µl was injected through the tail catheter to enhance contrast for capillary scans. Capillary scans were conducted using Linescan mode

of the TPM software with a 20x featuring a 1.0 N.A. and W.D. of 2.0 mm (UMPLFLN 20x, Olympus). Digital zoom was set to 5x, resulting in an *XY* pixel size of 0.23 μm. Capillaries were randomly selected, with efforts made to remain within the same FOV as used for indicator-dilution scans. A scan path was assigned in 1 – 5 capillaries, once in the axial direction of the capillary lumen for RBCv estimation, and twice transversally to the lumen for an averaged cell flux and capillary diameter (Fig. 4a). Line scan period varied between 0.5 to 2 ms per line. Scans were performed under steady-state conditions for 5 seconds.

4) Z-stacks for Aβ detection and angiograms: For detection of Aβ plaques, the day before to the scanning session, the mice were injected via I.P. with a dosage of 2 mg/kg of Methoxy-XO4 dye (Tocris Bioscience, Bristol, UK). In our setup, the excitation peak was at 790 nm, which was selected for the scanning sessions. The signal was filtered with a 460 ± 25 nm bandpass filter. For the detection of vessels, we labeled plasma with 200 μl of Texas-Red Dextran 70,000 MW (5 mg/ml, Thermo Fischer Scientific, Waltham, MA, USA). Excitation of Texas-Red Dextran was performed using a wavelength of 900 nm and emission was filtered with a 605 ± 35 bandpass filter.

Post-processing of indicator dilution techniques

MTT and CTH were estimated by modeling the tissue transport function (TF) through deconvolution following the injection of a dye bolus, as previously described[37]. For the analysis of the 2D time-series, we developed a dedicated MATLAB GUI that allowed the selection of vessels within the FOV. For modeling TF, it was crucial to select an arterial input function (AIF) and a venous output function (VOF). Initially, we identified pial arteries and veins as vessels positioned parallel to the cortex and without diving into the brain tissue. The main feeding arterial AIF was selected as the artery with the largest diameter and the shortest time-to-peak (TTP). Venous VOF was defined as the vein with the largest diameter and with the longest TTP. We identified the main arteriolar AIF as a vessel branching from an artery ($10 < d < 30$ μm), with the shortest TTP. The main venular VOF was defined as an ascending vessel ($10 < d < 60$ μm) with an anastomosis with a pial vein and with the longest TTP. The vascular TF described the relative amount of dye emerging at the VOF as a function of time after an idealized, instantaneous bolus injection on the

AIF. The TF was modeled by a gamma probability density function with parameters α and β, and a scaling factor, f. With this TF, we estimated MTT as the mean (α·β) and CTH as the standard deviation (√α·β). To visualize curve fitting and verify the MTT estimation, the AIF and VOF were compared after time-shifting the VOF curve by the estimated MTT (Supplementary Fig. 6). Bad curve fitting or curve-intensity saturation were used as criteria for rejection of analyzed pairs (Supplementary Fig. 7).

Post-processing of lifetime imaging for pO_2 measurements

To estimate pO_2, we determined the phosphorescence lifetime by fitting the phosphorescence intensity decay with a single-exponential function using the nonlinear least-squares method. The lifetime was converted to pO_2 using the calibration plot obtained in independent oxygen titration experiments[39]. For statistical analysis, we averaged the two measurements per vessel. To correlate oxygen tension to the diameter of the pial vasculature, segmentation, and diameter estimation were performed by two blinded research fellows averaging the distance of 5 transversal lines placed transversal to the vessel axis using the ROI manager plug-in of FIJI (Fig. 5c).

Post-processing of single capillary scans

Before processing, all images were filtered using a top-hat filter to improve SNR. RBCv, capillary cell flux, and diameter were calculated using a MATLAB GUI, as previously performed[37]. Briefly, RBCv was calculated from the axial capillary line scan using the Radon transform algorithm for analyzing streak angles (Figure 3a). Calculations were performed in 150 ms windows, displaced by 50 ms for each iteration. Cell flux was calculated by analyzing the intensity variations from the cross-section scan of each capillary (Figure 3a). Average intensity profiles were derived from 150-ms time interval windows within transversal line scans. A cluster analysis was applied to determine the presence of cells as they passed through the capillary. The capillary diameter was estimated from cross-sectional scans as the full width at half-maximum (FWHM) of intensity profiles within 150 ms windows, disregarding time intervals with the presence of RBCs.

Post-processing of angiograms for capillary morphometrics

The identification and segmentation of the capillary network involved the following steps:

1. Raw image stacks of the vasculature were first pre-processed using a Macro written in ImageJ (National Institutes of Health, Bethesda, Maryland, USA) for contrast enhancement and image denoising. The macro involved the following steps:

a) CLIJ2_equalizeMeanIntensitiesOfSlices for bleaching correction.
b) Contrast enhancement with normalization (saturated pixels = 0.4%).
c) Background subtraction (rolling ball = 50).
d) 3D Filtering (Median 3D; x = 2, y =2, z=2).

2. Vessel segmentation was performed using DeepVess, a deep convolutional neural network that enables the identification of individual capillary segments by extracting the vessel centerline[62].

3. Identification of capillary segments after segmentation was performed using a dedicated MATLAB script previously described[62]. Postprocessing included filtering according to diameter to remove the large vessels, with a set diameter limit of 8 pixels, equivalent to 9.2 µm (*XY* resolution = 1.15 µm per pixel).

4. Finally, another dedicated MATLAB script was employed to estimate the mean capillary diameter (Cap. Diameter) and standard deviation (SD) of each capillary segment, as well as capillary tortuosity as the Euclidean distance between two segment endpoints.

Additional parameters estimated: 1) Capillary diameter variance as the fraction of SD and Cap. Diameter; 2) Capillary length density as the total capillary length (µm) in the total z-stack volume (µl); and 2) Capillary blood volume as the fraction of the sum of capillary volumes (µl) and the total z-stack volume (µl).

Post-processing for Aβ deposits quantification

Aβ quantification was performed using a combination of Macros designed using ImageJ and Ilastik, an interactive machine learning for bioimage analysis[63].

A sub-stack of 100 slices (100 µm) was selected from a z-stack scanned with TPM to keep consistency between all groups. Contrast enhancement and denoising were performed using the same Macro as described for the angiograms and '.H5' files were saved for segmentation of plaques using the pixel classification workflow of Ilastik, which assigns labels based on pixel features and user annotations using a Random Forest classifier. The software was trained using two sub-stacks and the rest of the stacks were classified using the batch mode. Finally, for quantification of Aβ deposits, we use the '3D Objects Counter' from ImageJ, which gave the volume of each plaque across the sub-stack.

Extraction of tissue samples for molecular analyses

Following the last imaging session, mice underwent euthanasia by induction of deep anesthesia with isoflurane (4% in FiO_2 25%) and subsequent administration of an overdose of pentobarbital (100 mg/kg) intraperitoneally. Upon confirmation of respiratory arrest, a transcardial extraction of blood (300 – 500 µl) was performed. Plasma was recovered after centrifugation to remove the blood cells. Subsequently, the brain was carefully extracted from the skull of each mouse. The hippocampus and the region of the cortex of the scanned area were extracted (left hemisphere). All tissue samples were promptly snap-frozen and stored at –80°C until further preparation for molecular analyses.

Enzyme-linked immunosorbent assay (ELISA) to determine specific protein levels

The frozen tissue samples were finely minced on an aluminium plate cooled below 0 °C, and further homogenized by grinding in a 1.5 mL LoBind (Eppendorf) tube with a plastic pestle (GE Healthcare, Sample Grinding Kit), in 20 µL pr. mg tissue of an extraction buffer with 2% SDS, 100 mM sodium HEPES, and 1 cOmplete™ Protease Inhibitor Tablet (Roche) pr. 10 mL (1x PI). Finally, the sample was ultrasonicated for three cycles of five ultrasonication pulses on a Branson Sonifier 250 (Branson Ultrasonics Corporation) at output control 3 and 30% duty cycle. The protein content of each sample was measured in triplicates with the Pierce™ BCA Protein Assay Kit (Thermo Scientific) on a BSA standard curve according to the manufacturer's protocol.

Samples were diluted in extraction buffer to 2 µg protein/µL. To replace SDS with the ELISA compatible buffer Tween-20, SDS was precipitated was by addition of an equal

volume of a Tween/K buffer with 0.1% Tween-20, 100 mM $K2HPO_4$, 1×PI buffer followed by centrifugation for 15 minutes at 15,000×g at 2 °C, to pellet the potassium-SDS precipitate. The supernatant was aliquoted for each of the ELISAs and total protein content was determined, in triplicate, with the BCA assay.

For use in the ELISA standard curves, a sample buffer was prepared by precipitating SDS from the extraction buffer with the Tween/K buffer as described above.
All samples and standards were measured in duplicate. Absorbance was measured at 450 nm. The observed absorbance in the 0 standard, was subtracted from all measurements. A 4-parametric standard curve was applied to calculate specific protein concentrations. The average of the duplicates was multiplied by the dilution factor, and normalized to the total protein concentration of the sample after SDS-removal. The results are reported as pg-specific protein/mg total protein.

Aβ-40 was detected by an ELISA kit (Invitrogen, Cat. #: KHB3481) targeting human Aβ-40. Transgenic mice samples were diluted by a factor of 200 in the kit 'Standard Diluent Buffer'. The Aβ-40 standard was reconstituted in 55mM sodium bicarbonate, pH 9.0, according to protocol, and diluted from 100 ng/mL to the range of the standard curve (7.81-500 pg/mL) in a 1:199 mix of sample buffer and kit 'Standard Diluent Buffer'. The assay was otherwise run according to the manufacturer's protocol. The manufacturer reports a 0.5% cross-reactivity with rodent Aβ-40 which may explain the trace amount signal observed in some samples from WT mice, which were furthermore diluted only by a factor of 5.

For the detection of Aβ-42, we used an ELISA kit (Invitrogen, Cat. #: KHB3441) targeting human Aβ-42was employed. Samples were diluted by a factor of 5 in the kit 'Standard Diluent Buffer'. The Aβ-42standard was reconstituted and diluted in a 1:4 mix of sample buffer and kit 'Standard Diluent Buffer'. The assay was run otherwise according to the manufacturer's protocol.

For detection of Cyp- we used an ELISA kit (Abbexa, Cat. #: abx585050) targeting murine CypA. Samples were diluted by a factor ca 1.3 in the kit 'Standard Diluent Buffer' (80 µL

sample + 25 µL kit buffer). The CypA standard was reconstituted and diluted in a 3.8:1.2 mix of sample buffer and kit 'Standard Diluent Buffer'. Color development was allowed to proceed for 60 min. The assay was run otherwise according to the manufacturer's protocol.

ICAM-1 was detected using an ELISA kit (Abcam, Cat. #: ab100688) targeting murine ICAM1. Samples were diluted by a factor of 3.6 in the kit '1x Assay Diluent B' (28.5 µL sample + 103.5 µL kit buffer). The ICAM1 standard was reconstituted and diluted in a 30:11.4 mix of sample buffer and kit 'Standard Diluent Buffer'. The assay was run otherwise according to the manufacturer's protocol.

Mesoscale Discovery

Quantification of VEGF-A in plasma samples (1:1) obtained from scanned animals was conducted using the U-Plex Mouse VEGF-A Mesoscale Assay (Mesoscale Discovery, Rockville, USA) based on electrochemiluminescence. The procedure adhered to the standard protocol recommended by the manufacturer for preparation and measurements.

Ex-vivo MRI

An independent sample of mice was used for ex-vivo MRI scans. Four experimental groups were studied: WT mice (C57BL/6J, N=8 (F = 3, M = 5)], Tg-SwDI mice treated with MTZ (Tg+MTZ, N=12 (F = 7, M = 5)], Tg-SwDI mice treated with ATZ (Tg+ATZ, N=9 (F = 5, M = 4)] and Tg-SwDI mice treated with placebo (Tg-SwDI, N=9 (F = 3, M = 5).

Upon euthanasia, mice underwent perfusion-fixation with heparin (10 U·mL−1)-treated 0.9% saline (pH = 7.3) for 2 minutes, followed by ice-cold 4% buffered paraformaldehyde (PFA, pH = 7.2–7.4) for 2 min. Subsequently, the brain was removed from the skull and placed in PFA for extended fixation. In preparation for imaging, samples were washed in phosphate-buffered saline (PBS, Sigma USA, P4417- 50TAB) for a minimum of 24 hours to improve the signal by removal of excess fixative. The sample was then securely placed in an MRI-suitable tube filled with fluorinert (FC-770, 3M inc.) as is standard[64].

MRI was conducted using a Bruker Biospec 9.4T preclinical MRI system (Bruker Biospin, Ettlingen, Germany) equipped with a bore-mounted 15 mm volume coil. High-resolution structural data for volumetric estimation was acquired at 150 µm in-plane resolution in 200µm thick slices using a segmented (8 segments) T2-weighted echo planar imaging (EPI) sequence. Scan parameters were 16 avs, TE=31.7 ms, TR = 4500 ms, BW= 277 kHz, 70 axial slices. Regions of interest (i.e., cortex, somatosensory cortex (SMS), hippocampus (HC), and white matter WM) were manually segmented using ITK-SNAP, as shown previously[64].

Statistical analysis

We used R version 4.03 to perform statistical analysis and plots. For behavioral analysis and MRI analysis, an analysis of variance (ANOVA) was conducted to determine if there were any overall significant differences among the groups (WT, TgSwDI, Tg+ATZ, Tg+MTZ) and sex (females, males), between-subject factors. To compare the WT to all Tg groups, we performed a Dunnett's test to compare to a single control group. For group comparison between Tg groups, we performed post-hoc Tukey's test for multiple comparisons. In all analyses of optical imaging data, outliers were identified by calculating the z-score of each variable and removing data with a z-score below 3.29 or above 3.29, as previously described. We used the lme4 package for linear mixed-effect model estimates and constructed models with the hemodynamic parameter (e.g., cumulative stalling time, MTT, CTH), and group as fixed effects. We set intercepts for subjects as random effects. To examine the effect of gender, we constructed the same model integrating gender as fixed effect. Both models were compared by likelihood ratio test of the model with gender effect against the model without gender effect. In case the model with gender effect showed a significant difference against the model without gender effect, the hemodynamic effect was adjusted by gender. Comparison between groups was achieved by reordering the group level in each mixed model. The results in the tables are presented as mean ± S.D.

Acknowledgement

This work is supported through the Alzheimer's Association, (AARF-18-564411 to E.G.J.), the VELUX Foundation (ARCADIA II Grant 0026167 to E.G.J, L.Ø.), Lundbeck Foundation

(BRAIN COMET, R310-2018-3455 to E.G.J., L.Ø., P.M., I.K.M.), NIH USA grants (U24EB028941 to S.V. and NIH R01NS104127 and R01AG062572 to S.F., E.C.), and the Karen Toffler Charitable Trust Scholarship to E.C.. We also would like to thank Morten Frank Andersen for his support in segmenting the MRI data and Claudia Martinez for segmenting pial vessels from TPM data. We also thank Susanne S. Christensen and Anna Bay for their technical support and administration of the laboratory resources.

Authors contributions

EGJ, SF, and LØ conceived the study. EGJ established the study objectives, designed and performed the experiments, acquired, and processed TPM data, statistical analysis, and wrote the first draft of the manuscript. PMR, IKM, and SS set up and optimized TPM imaging processing software, supported in establishing TPM sequences and interpretation of data analysis. Further, PMR supported in statistical analysis. SK and DB supported in OCT acquisition software and imaging post-processing. SF supported in training of mice and scanning sessions. BH performed, analyzed, and interpreted MRI imaging. LB established awake imaging in the laboratory and monitoring software together with EGJ and SF. MEK and SV synthesized and calibrated the oxygen probe PtP-C343. JC and JP performed molecular biology tests, data analysis and interpretation. JRC reviewed data analysis, the manuscript and supported in interpretation of data. BW and DLG performed analysis of OCT data. EC, ACM, and BGL performed behavior tests and processing of behavior data. SF contributed to study objectives, experimental design, interpretation of data and critically reviewed the manuscript. LØ mentored EGJ and contributed to the study design, objectives, and interpretation of data and critically evaluated the manuscript.

Conflict of interest statement

The authors declare no conflict of interest. Silvia Fossati is an inventor on US Patent 10780094 for the use of CAIs in Alzheimer's disease and CAA. All other authors have nothing to disclose in relation to this study.

Data and code availability

The raw data used to generate all the figures shown in this paper are provided as a Source Data file. The imaging data generated in this study have been deposited in the

DataDryad database. All analysis codes used for statistical analyses and the generation of plots in MATLAB are available in the Zenodo.

References

1. Alzheimer's Disease International (ADI), Wimo, A., Prince, M. & International, A. D. World Alzheimer Report 2015, The Global Impact of Dementia. *Alzheimer's Disease International (ADI)* (2015) doi:10.1111/j.0963-7214.2004.00293.x.
2. Europe, A. Dementia in Europe Yearbook 2019 Estimating the prevalence of dementia in Europe. (2020).
3. Jack, C. R. *et al.* Tracking pathophysiological processes in Alzheimer's disease: an updated hypothetical model of dynamic biomarkers. *The Lancet Neurology* **12**, 207–216 (2013).
4. Aisen, P. S. *et al.* On the path to 2025: understanding the Alzheimer's disease continuum. *Alz Res Therapy* **9**, 60 (2017).
5. Bateman, R. J. *et al.* Two Phase 3 Trials of Gantenerumab in Early Alzheimer's Disease. *N Engl J Med* **389**, 1862–1876 (2023).
6. Van Dyck, C. H. *et al.* Lecanemab in Early Alzheimer's Disease. *N Engl J Med* **388**, 9–21 (2023).
7. Rabin, J. S. *et al.* Cerebral amyloid angiopathy interacts with neuritic amyloid plaques to promote tau and cognitive decline. *Brain* **145**, 2823–2833 (2022).
8. Iturria-Medina, Y. *et al.* Early role of vascular dysregulation on late-onset Alzheimer's disease based on multifactorial data-driven analysis. *Nature Communications* **7**, 1–14 (2016).
9. Iadecola, C. The overlap between neurodegenerative and vascular factors in the pathogenesis of dementia. *Acta Neuropathologica* **120**, 287–296 (2010).
10. Carey, A. & Fossati, S. Hypertension and hyperhomocysteinemia as modifiable risk factors for Alzheimer's disease and dementia: New evidence, potential therapeutic strategies, and biomarkers. *Alzheimer's & Dementia* **19**, 671–695 (2023).
11. Gutiérrez-Jiménez, E. *et al.* Disturbances in the control of capillary flow in an aged APPswe/PS1ΔE9 model of Alzheimer's disease. *Neurobiology of Aging* **62**, 82–94 (2018).

12. Wierenga, C. E., Hays, C. C. & Zlatar, Z. Z. Cerebral Blood Flow Measured by Arterial Spin Labeling MRI as a Preclinical Marker of Alzheimer's Disease. *Journal of Alzheimer's disease : JAD* **42**, S411 (2014).
13. Nation, D. A. *et al.* Blood-brain barrier breakdown is an early biomarker of human cognitive dysfunction. *Nature Medicine* **25**, 270–276 (2019).
14. Iadecola, C. The Pathobiology of Vascular Dementia. *Neuron* **80**, 844–866 (2013).
15. Soto-Rojas, L. O. *et al.* Molecular Sciences The Neurovascular Unit Dysfunction in Alzheimer's Disease. (2021) doi:10.3390/ijms22042022.
16. Jespersen, S. N. & Østergaard, L. The roles of cerebral blood flow, capillary transit time heterogeneity, and oxygen tension in brain oxygenation and metabolism. *Journal of Cerebral Blood Flow and Metabolism* **32**, 264–277 (2012).
17. Cruz Hernández, J. C. *et al.* Neutrophil adhesion in brain capillaries reduces cortical blood flow and impairs memory function in Alzheimer's disease mouse models. *Nature Neuroscience* **22**, 413–420 (2019).
18. Nortley, R. *et al.* Amyloid β oligomers constrict human capillaries in Alzheimer's disease via signalling to pericytes. *bioRxiv* Preprint at https://doi.org/10.1101/357095 (2018).
19. Østergaard, L. *et al.* The capillary dysfunction hypothesis of Alzheimer's disease. *Neurobiology of Aging* **34**, 1018–1031 (2013).
20. Nielsen, R. B. *et al.* Impaired perfusion and capillary dysfunction in prodromal Alzheimer's disease. *Alzheimer's & Dementia: Diagnosis, Assessment & Disease Monitoring* **12**, (2020).
21. Madsen, L. S. *et al.* Capillary dysfunction in healthy elderly *APOE ε* 4 carriers with raised brain Aβ deposition. *Alzheimer's & Dementia* **20**, 459–471 (2024).

22. Cvenkel, B. & Kolko, M. Current Medical Therapy and Future Trends in the Management of Glaucoma Treatment. *Journal of Ophthalmology* **2020**, 1–14 (2020).
23. Grissom, C. K., Roach, R. C., Sarnquist, F. H. & Hackett, P. H. *Acetazolamide in the Treatment of Acute Mountai n Sickness: Clinical Efficacy and Effect on Gas Exchange C. Annals of Internal Medicine* vol. 116 461–465 (1992).
24. Fossati, S. *et al.* The carbonic anhydrase inhibitor methazolamide prevents amyloid beta-induced mitochondrial dysfunction and caspase activation protecting neuronal and glial cells in vitro and in the mouse brain. *Neurobiology of Disease* **86**, 29–40 (2016).
25. Anzovino, A. *et al.* Amyloid Beta Oligomers Activate Death Receptors and Mitochondria-Mediated Apoptotic Pathways in Cerebral Vascular Smooth Muscle Cells; Protective Effects of Carbonic Anhydrase Inhibitors. *Cells* **12**, 2840 (2023).
26. Lemon, N., Canepa, E., Ilies, M. A. & Fossati, S. Carbonic Anhydrases as Potential Targets Against Neurovascular Unit Dysfunction in Alzheimer's Disease and Stroke. *Frontiers in Aging Neuroscience* **13**, 1–19 (2021).
27. Solesio, M. E. *et al.* Carbonic anhydrase inhibition selectively prevents amyloid β neurovascular mitochondrial toxicity. *Aging Cell* **17**, (2018).
28. Canepa, E. *et al.* FDA-approved carbonic anhydrase inhibitors reduce amyloid β pathology and improve cognition, by ameliorating cerebrovascular health and glial fitness. *Alzheimer's & Dementia* alz.13063 (2023) doi:10.1002/alz.13063.
29. Setti, S. E., Flanigan, T., Hanig, J. & Sarkar, S. Assessment of sex-related neuropathology and cognitive deficits in the Tg-SwDI mouse model of Alzheimer's disease. *Behavioural Brain Research* **428**, 113882 (2022).
30. Hébert, F. *et al.* Cortical atrophy and hypoperfusion in a transgenic mouse model of Alzheimer's disease. *Neurobiology of Aging* **34**, 1644–1652 (2013).

31. Ali, M. *et al.* VEGF signalling causes stalls in brain capillaries and reduces cerebral blood flow in Alzheimer's mice. *Brain* **145**, 1449–1463 (2022).
32. Erdener, Ş. E. *et al.* Spatio-temporal dynamics of cerebral capillary segments with stalling red blood cells. *Journal of Cerebral Blood Flow and Metabolism* **39**, 886–900 (2019).
33. Munting, L. P. *et al.* Cerebral blood flow and cerebrovascular reactivity are preserved in a mouse model of cerebral microvascular amyloidosis. *eLife* **10**, e61279 (2021).
34. Nortley, R. *et al.* Amyloid b oligomers constrict human capillaries in Alzheimer's disease via signaling to pericytes. *Science* **365**, (2019).
35. Østergaard, L. *et al.* Capillary Dysfunction: Its Detection and Causative Role in Dementias and Stroke. *Current Neurology and Neuroscience Reports* **15**, 37 (2015).
36. Mouridsen, K., Hansen, M. B., Østergaard, L. & Jespersen, S. N. Reliable estimation of capillary transit time distributions using DSC-MRI. *Journal of Cerebral Blood Flow and Metabolism* **34**, 1511–1521 (2014).
37. Gutiérrez-Jiménez, E. *et al.* Effect of electrical forepaw stimulation on capillary transit-time heterogeneity (CTH). *Journal of Cerebral Blood Flow and Metabolism* (2016) doi:10.1177/0271678X16631560.
38. Rasmussen, P. M., Jespersen, S. N. & Østergaard, L. The effects of transit time heterogeneity on brain oxygenation during rest and functional activation. *Journal of Cerebral Blood Flow and Metabolism* (2015) doi:10.1038/jcbfm.2014.213.
39. Finikova, O. S. *et al.* Oxygen Microscopy by Two-Photon-Excited Phosphorescence. *Chemphyschem* **9**, 1673–1679 (2008).
40. Sakadžić, S. *et al.* Two-photon high-resolution measurement of partial pressure of oxygen in cerebral vasculature and tissue. *Nature Methods* (2010) doi:10.1038/nmeth.1490.

41. Sakadžić, S. *et al.* Large arteriolar component of oxygen delivery implies a safe margin of oxygen supply to cerebral tissue. *Nature Communications* **5**, (2014).
42. Lu, X. *et al.* A Pilot Study Investigating Changes in Capillary Hemodynamics and Its Modulation by Exercise in the APP-PS1 Alzheimer Mouse Model. *Frontiers in Neuroscience* **13**, (2019).
43. Bell, R. D. *et al.* Apolipoprotein e controls cerebrovascular integrity via cyclophilin A. *Nature* **485**, 512–516 (2012).
44. Li, B. *et al.* More homogeneous capillary flow and oxygenation in deeper cortical layers correlate with increased oxygen extraction. *eLife* (2019) doi:10.7554/eLife.42299.
45. Harik, S. I., Hritz, M. A. & LaManna, J. C. Hypoxia-induced brain angiogenesis in the adult rat. *J Physiol* **485 (Pt 2)**, 525–530 (1995).
46. Chi, N. F., Chien, L. N., Ku, H. L., Hu, C. J. & Chiou, H. Y. Alzheimer disease and risk of stroke: A population-based cohort study. *Neurology* **80**, 705–711 (2013).
47. Gottesman, R. F. *et al.* Association between midlife vascular risk factors and estimated brain amyloid deposition. *JAMA - Journal of the American Medical Association* **317**, 1443–1450 (2017).
48. Eskildsen, S. F. *et al.* Increased cortical capillary transit time heterogeneity in Alzheimer's disease: a DSC-MRI perfusion study. *Neurobiology of Aging* **50**, 107–118 (2017).
49. Lu, X. *et al. Voluntary Exercise Increases Brain Tissue Oxygenation and Spatially Homogenizes Oxygen Delivery in a Mouse Model of Alzheimer's Disease*. *Neurobiology of Aging* vol. 88 (Elsevier Inc., 2020).
50. Madsen, L. S. *et al.* Capillary dysfunction correlates with cortical amyloid load in early Alzheimer's disease. *Neurobiology of Aging* **123**, 1–9 (2023).

51. Lu, X., Moeini, M., Li, B., Thorin, É. & Lesage, F. Hypertension accelerates cerebral tissue PO2 disruption in Alzheimer's disease. *Neuroscience Letters* **715**, 134626 (2020).

52. Roy, T. K. & Secomb, T. W. Functional implications of microvascular heterogeneity for oxygen uptake and utilization. *Physiological Reports* **10**, e15303 (2022).

53. 2 - Biomechanics of Microcirculation. in *Integrated Nano-Biomechanics* (eds. Yamaguchi, T., Ishikawa, T. & Imai, Y.) 9–69 (Elsevier, Boston, 2018). doi:https://doi.org/10.1016/B978-0-323-38944-0.00002-4.

54. Schmid, F., Reichold, J., Weber, B. & Jenny, P. The impact of capillary dilation on the distribution of red blood cells in artificial networks. *American Journal of Physiology-Heart and Circulatory Physiology* **308**, H733–H742 (2015).

55. Lee, J.-H. *et al.* Investigating the correlation between early vascular alterations and cognitive impairment in Alzheimer's disease in mice with SD-OCT. *Biomed. Opt. Express* **14**, 1494 (2023).

56. Provensi, G. *et al.* A new kid on the block? Carbonic anhydrases as possible new targets in alzheimer's disease. *International Journal of Molecular Sciences* **20**, (2019).

57. Gonzales, J. U. & Scheuermann, B. W. Effect of acetazolamide on respiratory muscle fatigue in humans. *Respiratory Physiology & Neurobiology* **185**, 386–392 (2013).

58. Meekers, E. *et al.* Renal function and decongestion with acetazolamide in acute decompensated heart failure: the ADVOR trial. *European Heart Journal* **44**, 3672–3682 (2023).

59. Park, L. *et al.* Age-dependent neurovascular dysfunction and damage in a mouse model of cerebral amyloid angiopathy. *Stroke; a journal of cerebral circulation* **45**, 1815–1821 (2014).

60. Desjardins, M. *et al.* Awake Mouse Imaging: From Two-Photon Microscopy to Blood Oxygen Level–Dependent Functional Magnetic Resonance Imaging. *Biological Psychiatry: Cognitive Neuroscience and Neuroimaging* **4**, 533–542 (2019).

61. Srinivasan, V. J. *et al.* Rapid volumetric angiography of cortical microvasculature with optical coherence tomography. *Optics Letters* **35**, 43 (2010).

62. Haft-Javaherian, M. *et al.* Deep convolutional neural networks for segmenting 3D in vivo multiphoton images of vasculature in Alzheimer disease mouse models. *PLOS ONE* **14**, e0213539 (2019).

63. Berg, S. *et al.* ilastik: interactive machine learning for (bio)image analysis. *Nature Methods 2019 16:12* **16**, 1226–1232 (2019).

64. Ardalan, M. *et al.* Reelin cells and sex-dependent synaptopathology in autism following postnatal immune activation. *British J Pharmacology* **179**, 4400–4422 (2022).

Figures and legends

Figure 1. Early amyloidosis and cortical hypertrophy in cognitively normal TgSwDI mice.a. Analysis of Barnes maze in WT and Tg-SwDI mice with and without treatment. WT n=12 (female 6, male: 6); Tg-SwDI n=15 (female 5 and male 10); Tg+ATZ n=13 (female 5, male 8); Tg+MTZ n=12 (female 6, male 6). Plots represent the number of mistakes (left), and distance covered (right). b. Analysis of open field to assess locomotor activity. WT n=12 (female 6, male: 6); Tg-SwDI, n=15 (female 5, male 10); Tg+ATZ, n=14 (female 6, male 8); Tg+MTZ, n=16 (female 8, male 8). Plots represent travelled distance (left), moving time (middle), and time spent on field's center (right). Significant difference between groups in travelled distance was observed (F [3, 53] = 3.539 cm, p = 0.0206). Post-hoc analysis (Dunnett's test): WT vs. Tg-SwDI, p = 0.035; WT vs. Tg+ATZ, p = 0.010; WT vs. Tg+MTZ, p = 0.045. c. Regional atrophy was assessed estimating regional tissue volume using ex-vivo MRI. Segmentation into cortex, hippocampus (HC), somatosensory area (SMS), and white matter (WM) was conducted. WT n=8 (5 males and 3 females); Tg-SwDI n=9 (6 males and 3 females); Tg+ATZ n=9 (4 males and 5 females); Tg+MTZ n=12 (5 males and 7 females). d. Plots for volume for each region. ANOVA showed difference across groups (F[3, 34] = 3.221 mm3, p = 0.0347). e. TPM Z-stacks (100 slides per ROI) of methoxy-positive amyloid deposits were pre-processed with ImageJ (left) and segmented using pixel classification of Ilastik (right). Tg-SwDI, n=28 (16 female and 12 male); Tg+ATZ, n=21 (12 females and 9 males); Tg+MTZ, n=24 (10 females and 14 males). f. Plot of Aβ plaque burden (%). g. Plot of plaque number per mm3. P-values: *p<0.05, **p≤0.01.

Figure 2. Long-lasting capillary stalling in the Tg-SwDI is prevented by CAIs. a. OCT-A was used to detect stalling events. WT n=11 (6 female and 5 male); Tg-SwDI n=18 mice (11 female and 7 male); Tg+ATZ n=17 mice (7 female and 10 male); Tg+MTZ n=15 (7 female and 8 male). MIP of 100 µm (axial) of an ROI (600 μm^2) with stalling segments indicated (red markings). **b.** Sixty OCT-A-volumes in 2 ROIs per mouse were performed (~8.5 seconds/volume). **c.** Magnification of selected region (cyan in a) with capillary segments (arrowheads) with temporary perfusion interruptions. Hollow arrowheads indicate a stalling event. **d.** Representative stall-o-grams from a ROI per group of stalling segments through 60 OCT-A-volumes. Black points represent stalling events per each image frame. **e**, Identified capillary stall events in each examined ROI. WT vs. Tg-SwDI, Linear mixed model (LMM), difference (diff.) = 4 ± 1 stalls, p = 0.03; WT vs. Tg+ATZ, LMM, diff. = 5 ± 2 stalls, p = 0.006. **f.** Incidence of capillary stalls. WT vs. Tg-SwDI, LMM, diff. = 2.52 ± 1.05 %, p = 0.02. WT vs. Tg+ATZ, LMM, diff. = 2.28 ± 1.06 %, p = 0.003 (n=116 in 61 mice). **g.** Prevalence as a percentage of stalling events per volume. WT vs. Tg-SwDI, LMM, diff. = 0.31 ± 0.11, p = 0.009; WT vs. Tg+ATZ, LMM, diff. = 0.25 ± 0.11, p = 0.03 (n=116, 61 mice); Tg-SwDI vs. Tg+MTZ, LMM, diff. = –0.23 ± 0.10, p = 0.03. **h.** Cumulative stall duration as percentage of time of each ROI (~8.5 minutes). Tg-SwDI vs. Tg+ATZ, LMM, diff. = –1.62 ± 0.8, p = 0.04; Tg-SwDI vs. Tg+MTZ, diff. = –2.49 ± 0.81, p = 0.003. n=116 ROIs, 61 mice). Scale bar = 100 µm. P-values: *p < 0.05, **p ≤ 0.01.

Figure 3. Disturbances in capillary flows and morphology are prevented in CAI-treated Tg-SwDI mice. a. Simultaneous estimation of RBCv, cell flux, capillary LD and capillary diameter (Cap. Diam.) from single-capillary scans. A path traversed the capillary longitudinally (red) and transversely (blue) were TPM linescans were performed (upper left). RBCv (*bottom left*) was calculated using the Radon transformation based on streak angles. Diameter (*bottom middle*) and cell flux (bottom *left*) were estimated from the transversal. A total of 583 capillaries were scanned across groups. Scale bar: 20 µm. **b.** Plot representing RBCv in each group. LMM were constructed to compare groups with mouse ID as random effect. **c.** Plot of the capillary cell flux. **d.** Plot for capillary linear density (Cell flux/RBCv). **e.** Plot of capillary diameter. **f.** Scatter plot illustrating the relationship between RBCv and capillary diameter. **g.** Scatter correlation illustrating the relationship between cell flux and capillary diameter. **h.** Plot of RBCv COV. **j.** Postprocessing of TPM angiograms using DeepVess. Each angiogram was composed of 100 slices, ~50 µm below the top layer. Each stack was pre-processed for contrast enhancement (*left*) and then segmented into binary images and vessel center lines using DeepVess (*middle and right*)[62] from where mean capillary segment diameter and standard deviation (SD) were estimated. Scale bar: 200 µm. Estimates were performed per mouse and per group. **k,** Plots for mean capillary segment diameter. **l.** Plots of mean capillary segment diameter SD. **m.** Plot of mean capillary length density. P-values: *p < 0.05, **p ≤ 0.01.

Figure 4. Capillary dysfunction is present in the Tg-SwDI but not in the treated mice with CAIs. a. Indicator-dilution method for estimating MTT and CTH in clinical settings using dynamic susceptibility contrast (DSC)-magnetic resonance imaging (MRI). Left: RTH maps (CTH/MTT) from two controls and two patients with different mini-mental scale evaluation (MMSE) scores predicting AD patients (Modified from Eskildsen et al.[48]) Maps of MTT and CTH are estimated in each voxel through parametric deconvolution[36] between an arterial input function (AIF, i.e., middle cerebral artery) and a residue function (signal residue after the passage of the contrast agent). In contrast, high-spatial resolution of TPM (Right) allows the selection of AIF (red range colors) and a venous output function (VOF; blue range colors) within the field-of-view. Scans involved the injection of 10 µl of fluorescent dye while performing spiral scans (~7 fps.). Scale bar: 100 µm. **b.** Intensity curves of vessels selected. A 10-s curve-matching region was selected to estimate MTT and CTH and all curves were normalized to the post-bolus baseline of the AIF. **c.** The probability transport function of capillary transit times h(t) was parameterized by a gamma variate with parameters α and β (MTT = α·β, CTH = √α·β). **d.** MTT and

CTH estimations between arteries and veins. LMM were constructed to compare effect of treatment in MTT, CTH. CTH in Tg-SwDI vs. WT group: Diff. = 0.15 ± 0.07, p 0.044. **e.** MTT and CTH estimations between arterioles and venules. CTH in Tg+MTZ vs. Tg+ATZ: Diff. = –0.20 ± 0.06, p = 0.002. CTH in Tg+ATZ vs. WT Diff. = 0.15 ± 0.06, p = 0.02; Tg+ATZ vs. Tg-SwDI group Diff. = 0.16 ± 0.06, p = 0.02. P-values: * p < 0.05, ** p ≤ 0.01.

Figure 5. Alterations in OEF are not present in pre-symptomatic Tg-SwDI mice. a. intravascular (I.V.) pO_2 was estimated using 2PLM by TPM after the I.V. injection of an oxygen-sensitive dye (PtP-C343). Single-point excitation was used, and photons were collected with a PMT and counted using time-correlated single-photon counting (TCSPC). Two single-point estimates were performed on each vessel from which MTT and CTH were estimated. **b.** PO_2 was determined by fitting phosphorescence intensity decay with a single-exponential function using nonlinear least-squares method. Lifetime was converted to pO_2 using a calibration plot from independent oxygen titration. Higher photon lifetime in arteries indicates higher O_2 concentration compared to veins. **c.** Manual vessel diameter segmentation of vessels where pO_2 was measured (5 lines per point). **d.** Diameter estimates from arterial networks. **e.** Arterial pO_2. WT vs. Tg+ATZ, LMM, diff. = -8.34 ± 3.86 mmHg, p = 0.03. **f.** Computed SO_2. Arteries: WT vs. Tg-SwDI, LMM, diff. = –0.034 ± 0.02, p = 0.03; WT vs. Tg+ATZ, LMM, diff. = –0.03 ± 0.01, p = 0.02; WT vs. Tg+MTZ, LMM, diff. = –0.03 ± 0.01, p = 0.04. Diving arterioles: WT vs. Tg+MTZ, LMM, diff. = –0.04 ± 0.02, p = 0.04. **g.** Diameter from venous networks. **h.** Venous pO_2. Venules: Tg+MTZ vs. Tg+ATZ, LMM, diff. = 5.60 ± 2.71 mmHg, p = 0.043. **i.** Venous SO_2. Tg+ATZ vs. Tg+MTZ, LMM, diff. = 0.08 ± 0.04, p = 0.045. **j.** OEF between pial arteries and veins (mean per mouse). Tg+ATZ vs. Tg+MTZ, LMM, diff. = 0.08 ± 0.04, p = 0.037. **k,** OEF between arterioles to venules. Tg-SwDI vs. Tg+MTZ, LMM, diff. = –0.10 ± 0.04, p = 0.016; Tg-SwDI vs. Tg+ATZ group, LMM, diff. = –0.11 ± 0.04, p < 0.01. Scale bar: 500 µm. P-values: *p < 0.05, **p ≤ 0.01.

Figure 6. Leukocyte adhesion molecules and BBB marker levels. a. Box plot of ICAM-1 levels in homogenized cortex and hippocampus, respectively, measured by ELISA. Significant difference between groups in ICAM-1 expression was observed in cortex (ANOVA, F[1, 3] = 10.046 pg/ml, p < 0.001) and hippocampus (F[1, 3] = 9.2224 pg/ml, p = 0.0019). Post-hoc analysis (Tukey's test) for group comparison (WT: n=12 (5 female, 7 male); Tg-SwDI: n=9 mice (5 female, 4 male); Tg+ATZ: n=9 mice (5 female, 4 male; Tg+MTZ: n=9 mice (5 female, 4 male). **b.** Box plot of CYP-A levels obtained from ELISA analyses of homogenized cortex and hippocampus and **c.** Box plot of levels VEGF-A in plasma measured by Mesoscale. P-values: *p < 0.05, **p ≤ 0.01, ***p ≤ 0.001.

Figure 7. Amyloid overload is reduced in cortex and hippocampus in CAI treated Tg-SwDI mice. a. Box plot of total Aβ-40 load measured by ELISA of homogenized cortex and hippocampus, respectively. Significant difference between groups was observed in Aβ-40 load in cortex (F1, 2] = 4.0646 pg/ml, p = 0.0307) and hippocampus (F1, 2] = 3.14e9 pg/ml, p = 0.0011). Post-hoc analysis (Tukey's test) for group comparison. **b.** Box plot of total Aβ-42 load in cortex and hippocampus. Significant difference between groups was observed in Aβ-42 load in cortex (F1, 2] = 10.239 pg/ml, p < 0.001) and hippocampus (F1, 2] = 6.9141 pg/ml, p = 0.0044). Post-hoc analysis (Tukey's test) for group comparison. P-values: *p < 0.05, **p ≤ 0.01, ***p ≤ 0.001.

Figure 8. Disturbances in capillary patterns in Tg-SwDI induce capillary dysfunction. a. In healthy capillary networks, the transport of oxygen between blood and tissue is limited by blood's capillary transit time and the distribution of capillary flows (thin yellow arrows) at a given time. Leukocytes commonly have a rounded shape with few adhesion bonds not affecting homogenization of capillary flows. **b.** Phenomena affecting capillary patency, such as lumen narrowing and stalling, can disturb capillary flow patterns. In AD narrowing is suggested to occur at regions where amyloid plaques are close to pericytes[18]. Consequently, leukocytes will need to squeeze through the capillaries, taking on a disk shape and increasing the number of adhesion bonds, which promotes capillary stalling. These pathological phenomena induce shunting of capillary flows through low-resistance capillaries (thick yellow paths/arrows) and prevent their normal homogenization (increased CTH), leading to capillary dysfunction during increases in blood flow.

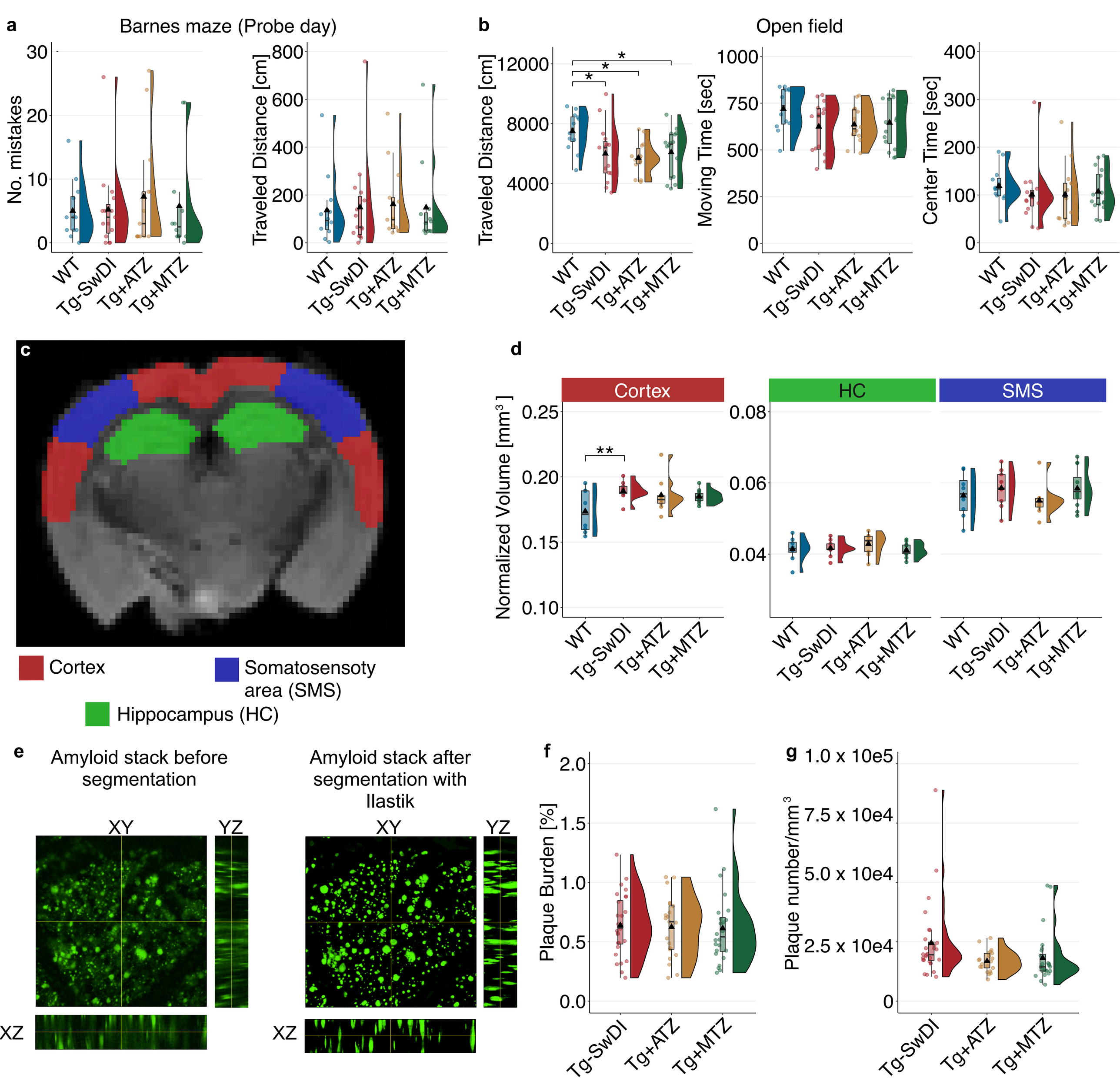
a
Barnes maze (Probe day)
No. mistakes
Traveled Distance [cm]
WT
Tg-SwDI
Tg+ATZ
Tg+MTZ
b
Open field
Traveled Distance [cm]
Moving Time [sec]
Center Time [sec]
c
Cortex
Somatosensoty area (SMS)
Hippocampus (HC)
d
Cortex
HC
SMS
Normalized Volume [mm³]
e
Amyloid stack before segmentation
Amyloid stack after segmentation with Ilastik
XY
YZ
XZ
f
Plaque Burden [%]
g
Plaque number/mm³

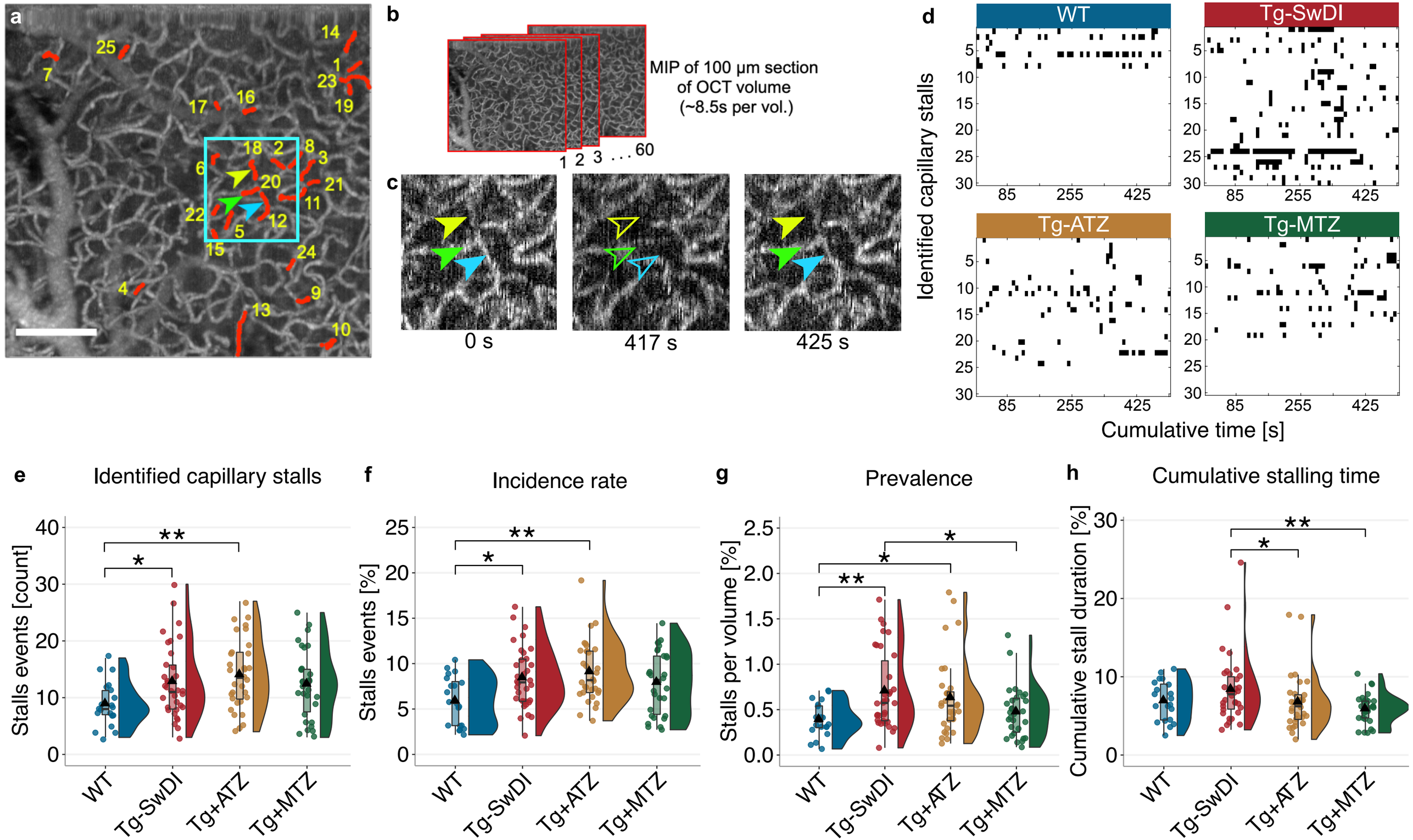
a
b
MIP of 100 µm section
of OCT volume
(~8.5s per vol.)
1 2 3 . . . 60
c
0 s
417 s
425 s
d
WT
Tg-SwDI
Tg-ATZ
Tg-MTZ
Identified capillary stalls
Cumulative time [s]
e
Identified capillary stalls
Stalls events [count]
f
Incidence rate
Stalls events [%]
g
Prevalence
Stalls per volume [%]
h
Cumulative stalling time
Cumulative stall duration [%]
WT
Tg-SwDI
Tg+ATZ
Tg+MTZ

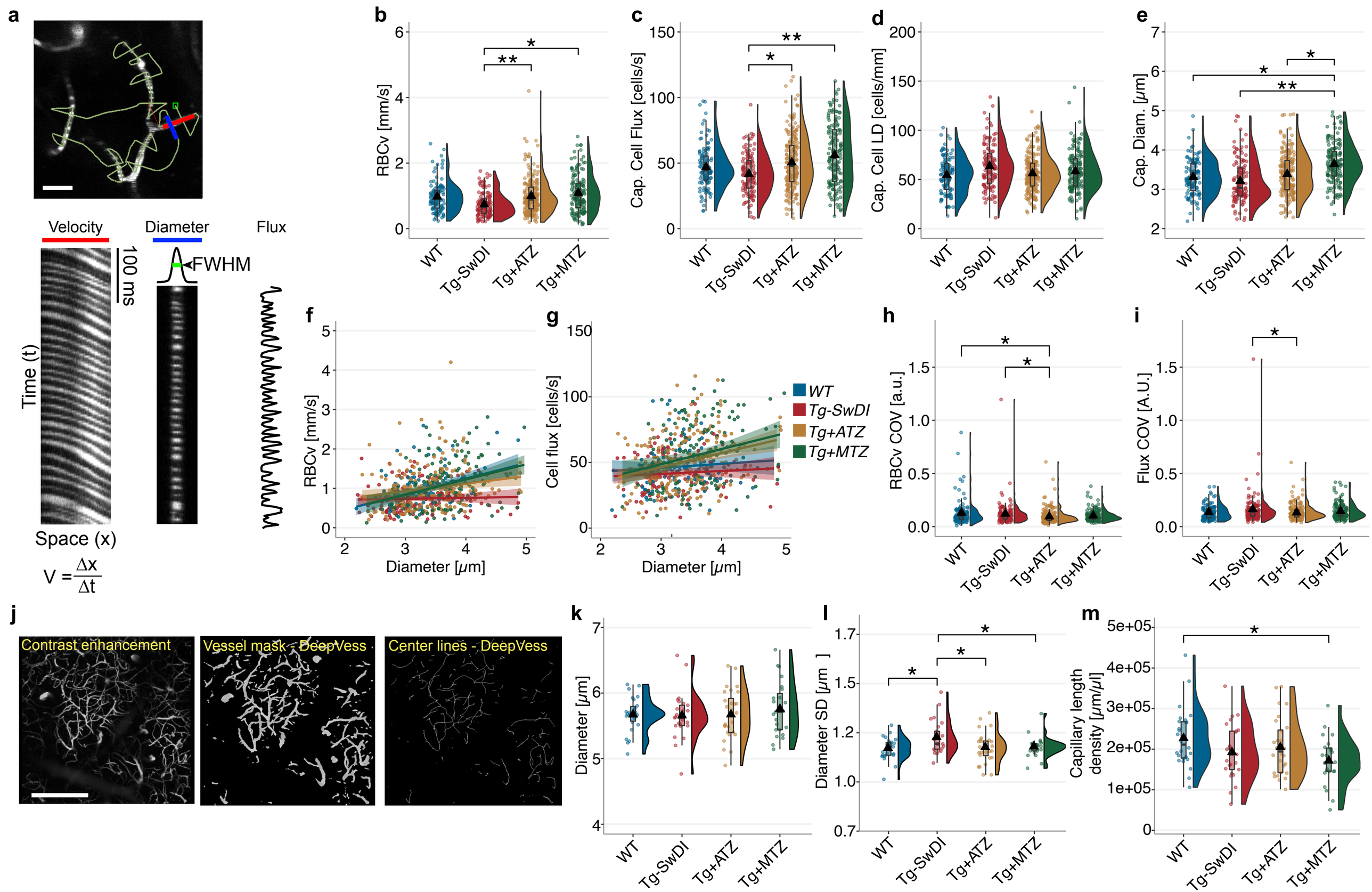
a
Velocity
Diameter
Flux
100 ms
FWHM
Time (t)
Space (x)
V = Δx/Δt
b
RBCv [mm/s]
WT
Tg-SwDI
Tg+ATZ
Tg+MTZ
c
Cap. Cell Flux [cells/s]
d
Cap. Cell LD [cells/mm]
e
Cap. Diam. [μm]
f
RBCv [mm/s]
Diameter [μm]
g
Cell flux [cells/s]
Diameter [μm]
WT
Tg-SwDI
Tg+ATZ
Tg+MTZ
h
RBCv COV [a.u.]
i
Flux COV [A.U.]
j
Contrast enhancement
Vessel mask - DeepVess
Center lines - DeepVess
k
Diameter [μm]
l
Diameter SD [μm]
m
Capillary length density [μm/μl]

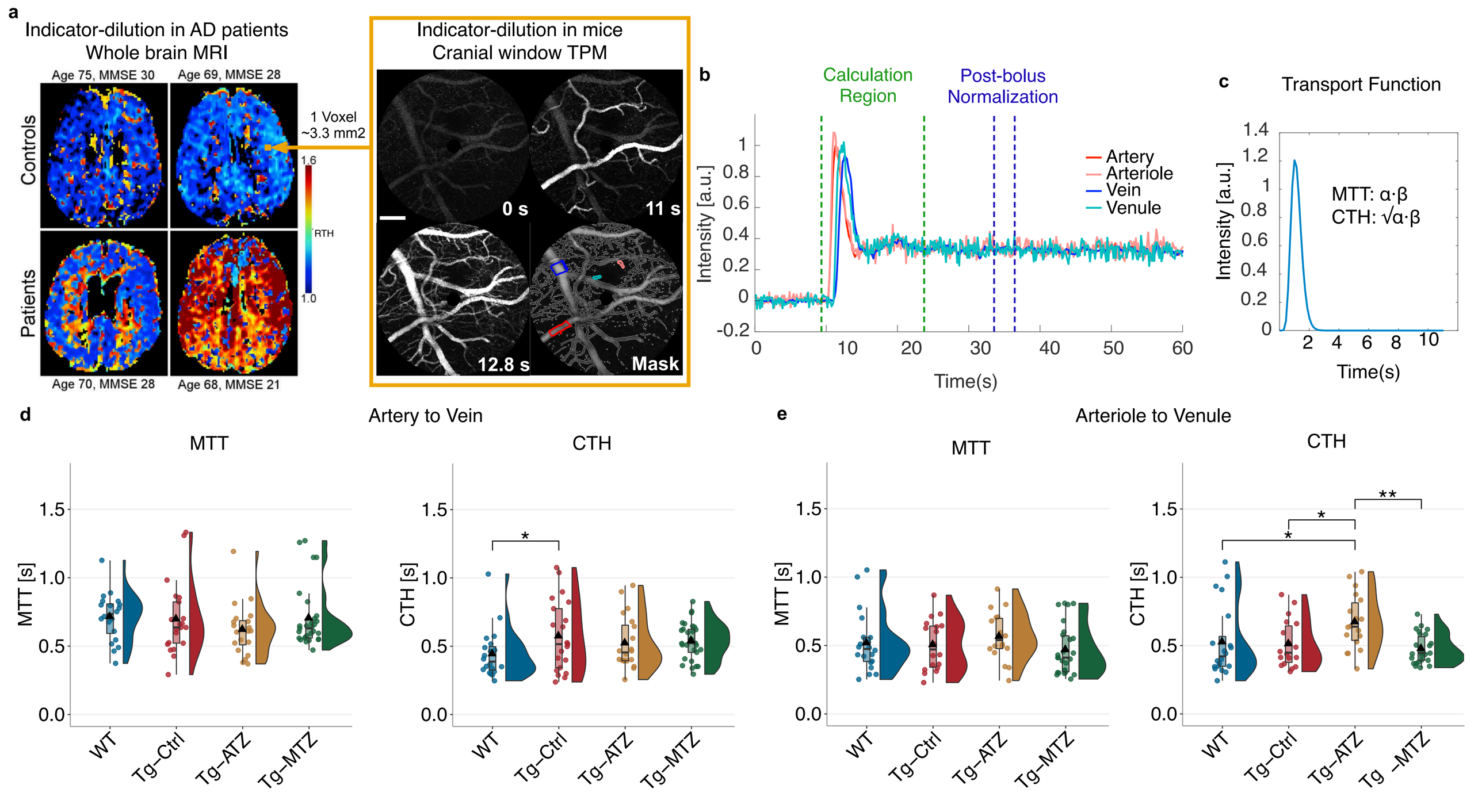
a
Indicator-dilution in AD patients
Whole brain MRI
Age 75, MMSE 30
Age 69, MMSE 28
Controls
Patients
Age 70, MMSE 28
Age 68, MMSE 21
1 Voxel
~3.3 mm2
1.6
RTH
1.0
Indicator-dilution in mice
Cranial window TPM
0 s
11 s
12.8 s
Mask
b
Calculation Region
Post-bolus Normalization
Artery
Arteriole
Vein
Venule
Intensity [a.u.]
Time(s)
c
Transport Function
MTT: α·β
CTH: √α·β
Intensity [a.u.]
Time(s)
d
Artery to Vein
MTT
CTH
MTT [s]
CTH [s]
WT
Tg–Ctrl
Tg–ATZ
Tg–MTZ
e
Arteriole to Venule
MTT
CTH
MTT [s]
CTH [s]
WT
Tg–Ctrl
Tg–ATZ
Tg–MTZ
Tg –MTZ

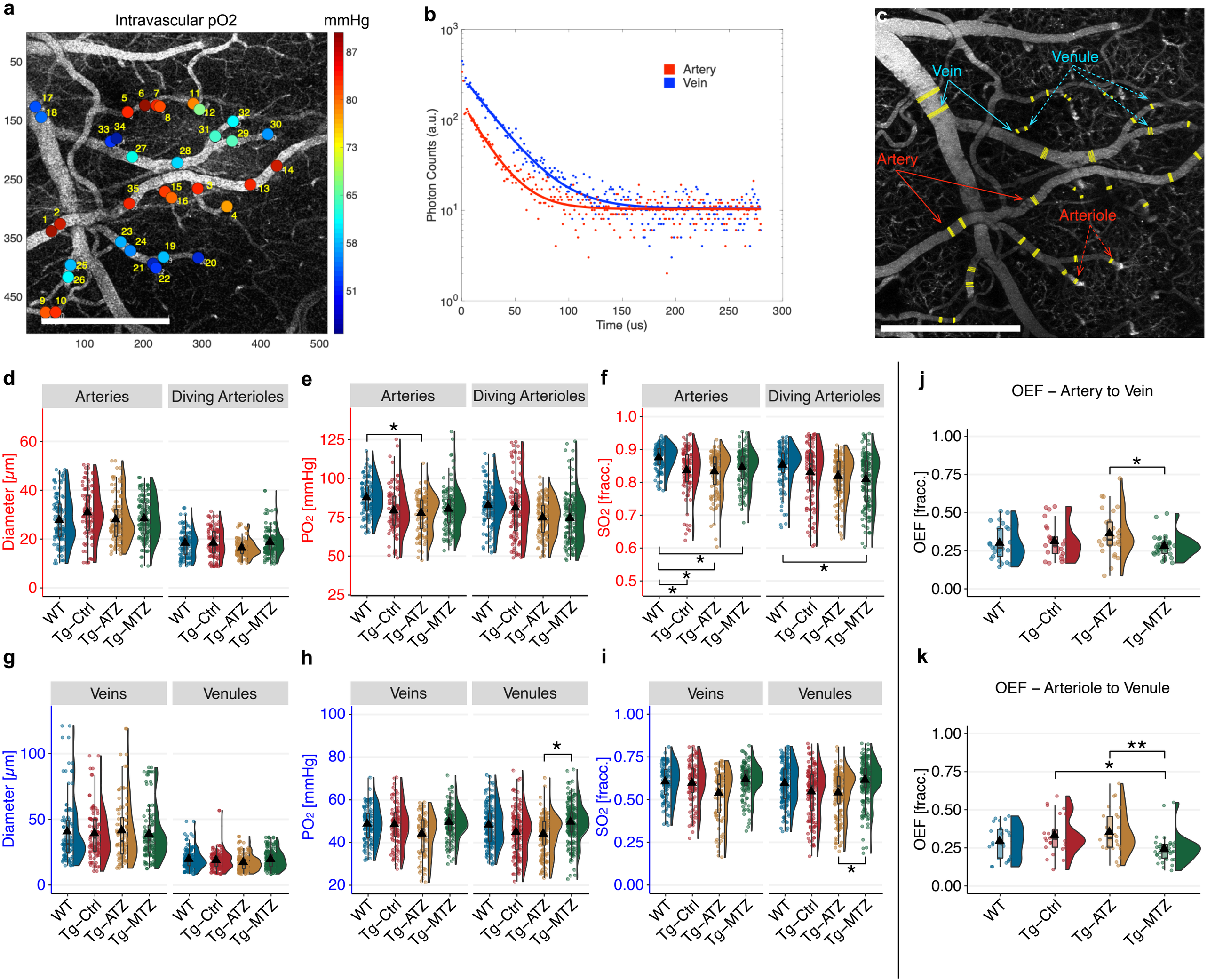
a
Intravascular pO2
mmHg
b
Photon Counts (a.u.)
Time (us)
Artery
Vein
c
Vein
Venule
Artery
Arteriole
d
Arteries
Diving Arterioles
Diameter [μm]
e
PO2 [mmHg]
f
SO2 [fracc.]
j
OEF – Artery to Vein
OEF [fracc.]
g
Veins
Venules
h
i
k
OEF – Arteriole to Venule
WT
Tg–Ctrl
Tg–ATZ
Tg–MTZ

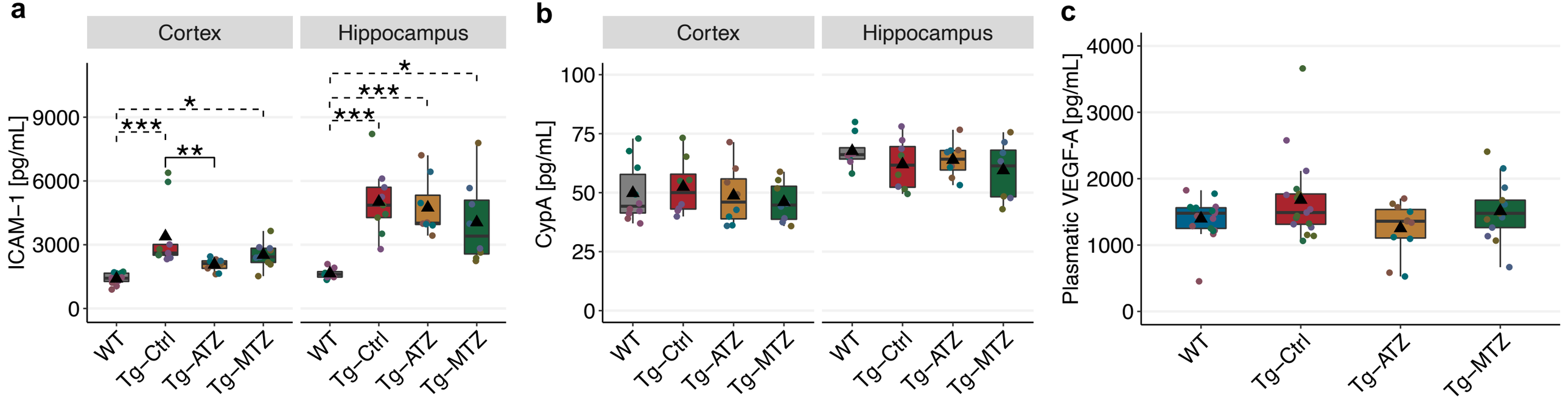
a
Cortex
Hippocampus
ICAM−1 [pg/mL]
9000
6000
3000
0
*
***
**
*
***
***
WT
Tg−Ctrl
Tg−ATZ
Tg−MTZ
b
Cortex
Hippocampus
CypA [pg/mL]
100
75
50
25
0
WT
Tg−Ctrl
Tg−ATZ
Tg−MTZ
c
Plasmatic VEGF-A [pg/mL]
4000
3000
2000
1000
0
WT
Tg−Ctrl
Tg−ATZ
Tg−MTZ

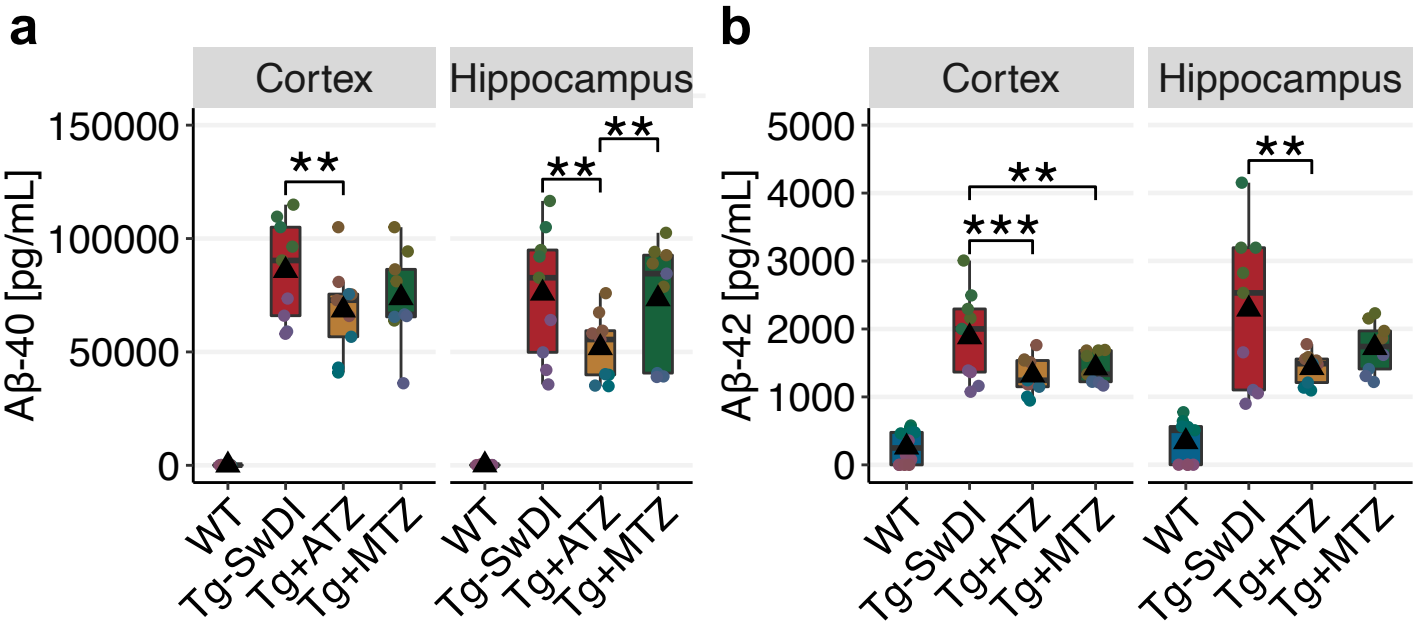
a
Cortex
Hippocampus
Aβ-40 [pg/mL]
150000
100000
50000
0
**
**
**
WT
Tg-SwDI
Tg+ATZ
Tg+MTZ
b
Cortex
Hippocampus
Aβ-42 [pg/mL]
5000
4000
3000
2000
1000
0
**
***
**
WT
Tg-SwDI
Tg+ATZ
Tg+MTZ

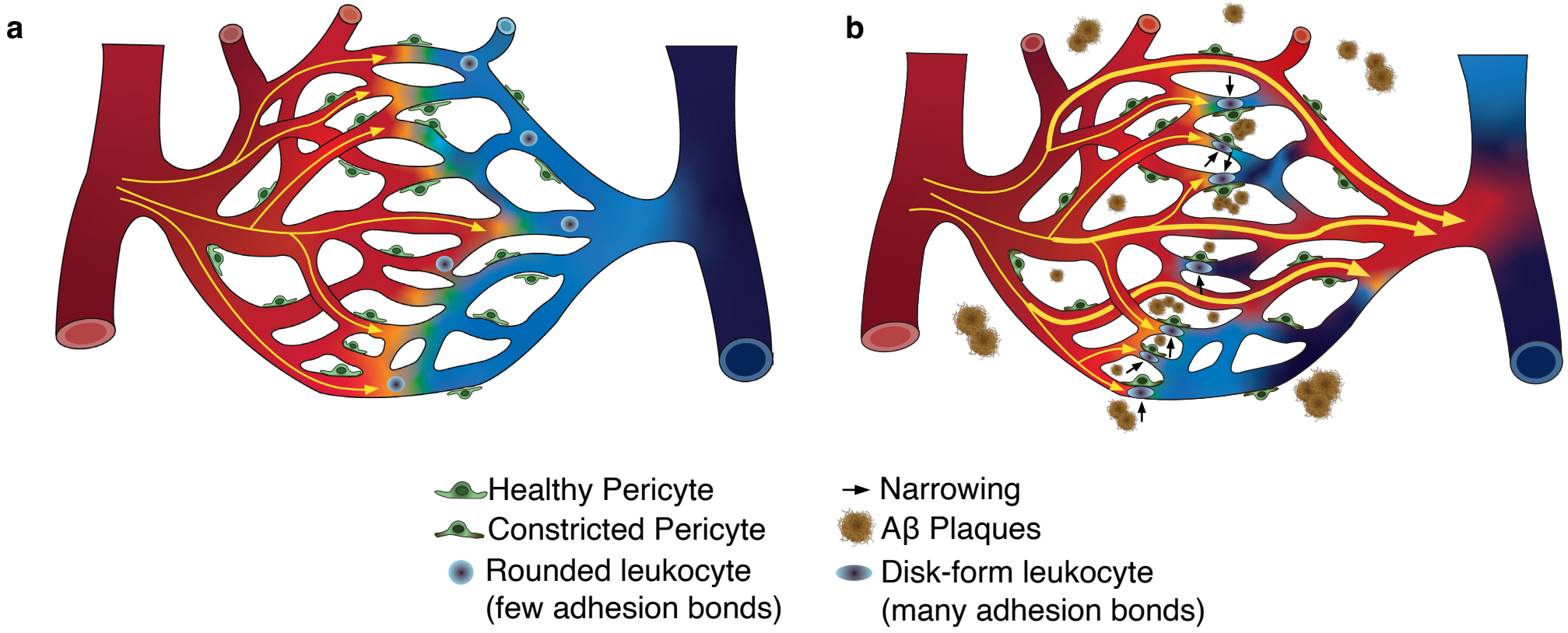
a
b
Healthy Pericyte
Constricted Pericyte
Rounded leukocyte
(few adhesion bonds)
Narrowing
Aβ Plaques
Disk-form leukocyte
(many adhesion bonds)